International Journal of Nanomedicine

Dovepress
Taylor & Francis Group

Open Access Full Text Article

ORIGINAL RESEARCH

Multi-Functional Magnetic Nanocrystals for Tumor Mitochondria-Targeted Magnetic Hyperthermia Combined with Enhanced Radiotherapy

Yue Zong[1,2], Jie He[1,2], Yichun Wu[1,2], Jingwen Qin[2], Mingyan Zhao[2], Xingyu Zhu[2], Jun Xie[2], Haitao Yin[3]

[1]Affiliated Xuzhou Clinical College of Xuzhou Medical University, Xuzhou, Jiangsu, 221009, People's Republic of China; [2]Key Laboratory for Biotechnology on Medicinal Plants of Jiangsu Province, School of Life Science, Jiangsu Normal University, Xuzhou, Jiangsu, 221116, People's Republic of China; [3]The Affiliated Xuzhou Municipal Hospital of Xuzhou Medical University, Xuzhou, Jiangsu, 221112, People's Republic of China

Correspondence: Haitao Yin; Jun Xie, Email yinhaitao@njmu.edu.cn; xiejun@jsnu.edu.cn

International Journal of Nanomedicine downloaded from https://www.dovepress.com/
For personal use only.

Objective: In this study, a fluorescent magnetic nanomaterial with mitochondrial targeting property (Fe_3O_4@DPPC@DMPE-PEG_{2000}-LOD@IR780, FDLI) was successfully prepared. We found that FDLI-mediated targeted magnetic hyperthermia (TMH) increases the sensitivity of tumor to radiotherapy (RT). The related underlying mechanisms have also been revealed.

Methods: The crystal structure, chemical composition, magnetic properties, optical characteristics and enzyme-like activity of FDLI were systematically elevated. The mitochondrial targeting ability, anti-tumor efficacy, and RT sensitization potential of FDLI were validated in vitro using breast cancer 4T1 cells. Additionally, a subcutaneous breast tumor transplantation mouse model was established to evaluate the therapeutic effectiveness of FDLI, and an optimized in vivo treatment protocol was assessed. Following intravenous administration of FDLI in mice, the diagnostic and therapeutic effects were evaluated using FDLI-mediated multimodal imaging diagnosis and therapeutic strategies.

Results: Following mitochondrial targeting of tumor cells, FDLI induced localized TMH and exhibited peroxidase-like activity to generate ·OH, which selectively disrupted the mitochondrial membranes of tumor cells, resulting in reduced adenosine triphosphate (ATP) production and elevated lipid peroxidation. Meanwhile, FDLI increased intracellular reactive oxygen species (ROS) levels while reducing glutathione (GSH) levels, thereby promoting ferroptosis in tumor cells and enhancing the sensitivity to synergistic RT.

Conclusion: FDLI can effectively inhibit tumor growth and metastasis, prolonging the survival of tumor-bearing mice through the combined effects of TMH and RT. Our study provides a clinical basis for the development of FDLI as a high-performance agent for integrated tumor diagnosis and therapy.

Keywords: magnetic induction hyperthermia, magnetic nanocrystals, mitochondrial targeting, ferroptosis, radiotherapy sensitisation, synergistic therapy

Introduction

Magnetic nanomaterials have recently become vital in the field of advanced nanomaterials.[1–3] They possess the typical mesoscopic characteristics of nanomaterials and unique mesoscopic magnetic properties and biocompatibility, which make them suitable for biomedical applications. Over the past three decades, the integrated model of tumor diagnosis and therapy mediated by magnetic nanomaterials has played a crucial role in the early detection and treatment of tumors.[4–6] This model integrates nanomaterials with drugs and employs multi-modal imaging to monitor the in vivo distribution of nanomaterials and drugs and the real-time localisation of tumors, providing guidance for multi-modal therapies and personalised treatment strategies for clinical practice. Notably, tumor hyperthermia is another important tumor treatment modality after surgery, radiotherapy (RT), chemotherapy and biological immunotherapy.[7–9] Among various hyperthermia technologies, targeted magnetic hyperthermia (TMH) based on magnetic nanomaterials has been developed as a novel tumor treatment approach.[10–12] Its underlying principle is as follows: under the influence of an external alternating

Received: 18 April 2025
Accepted: 28 August 2025
Published: 11 September 2025

© 2025 Zong et al. This work is published and licensed by Dove Medical Press Limited. The full terms of this license are available at https://www.dovepress.com/terms.php and incorporate the Creative Commons Attribution – Non Commercial (unported, v4.0) License (http://creativecommons.org/licenses/by-nc/4.0/). By accessing the work you hereby accept the Terms. Non-commercial uses of the work are permitted without any further permission from Dove Medical Press Limited, provided the work is properly attributed. For permission for commercial use of this work, please see paragraphs 4.2 and 5 of our Terms (https://www.dovepress.com/terms.php).

current magnetic field (ACMF), nano-magnetofluid is used as a formulation and the thermal effect is generated through magnetic spin relaxation, converting electromagnetic energy into thermal energy. When the magnetic fluid is targeted and transported into the tumor, the induced magnetic thermal effect increases the local temperature, leading to immediate metabolic reactions at the lesion site. Subsequently, the cellular structures are damaged, including the cell membrane, nuclear membrane, mitochondria and lysosomes. This induced cell apoptosis can inhibit tumor growth. As an innovative, safe and effective tumor treatment, TMH has been applied to various tumor models.[13–15]

Different hyperthermia temperatures play a decisive role in TMH's healing effect on tumors. Increasing this temperature within the tumor to 41°C–46°C can affect the function and status of tumor cell membranes, activate lysosome activity and suppress the synthesis of DNA, RNA and protein, thereby inducing cell apoptosis.[16,17] This method is classified as mild hyperthermia. When the temperature exceeds 50°C, tumor cells can be directly killed, causing the necrosis, coagulation and scab shedding of malignant tumor tissues.[18–21] This phenomenon is known as thermal ablation or resection. A comparison of the above hyperthermia methods reveals that thermal ablation or resection can suppress tumors in a short period but has a risky and strong killing effect on tumor and normal cells. By contrast, mild hyperthermia requires a longer treatment period but is safer and is commonly used to enhance tumor tissue sensitivity to RT and chemotherapy. In clinical applications, fully considering the potential toxic side effects of hyperthermia and rationally selecting the appropriate dose of hyperthermia are crucial for ensuring the clinical safety of TMH.[22]

Ideally, in TMH, the nanomaterials should remain confined to tumor tissues to avoid accumulation in other organs. Therefore, the surface of magnetic nanoparticles has been modified with targeting molecules (such as PEG, phospholipids, folic acid, transferrin, RGD peptides and other targeting antigens or receptors) to utilise their targeting properties for precise delivery to the target sites.[23–30] Additionally, the concentration of nanoparticles within the tumor has been remarkably increased to effectively realise hyperthermia within the tumor tissue or cells, leading to the improved efficacy of TMH. Mitochondria are the energy factory of cells and the main site of the cellular oxidative respiratory chain.[31–33] They are also involved in biological processes such as cell information transmission, cell differentiation and control of cell cycle and growth. In recent years, mitochondria have become an important target in drug development. By regulating intracellular reactive oxygen species (ROS), Ca^{2+} and lipid peroxidation (LPO) levels, mitochondria can interact with the endoplasmic reticulum to induce endoplasmic reticulum stress and promote apoptosis, making them one of the research hotspots in tumor-targeted therapy.[34,35] As a near-infrared lipophilic molecular probe that targets mitochondria, IR780 possesses acoustic and optical sensitivities.[36,37] Owing to its advantages of strong mitochondrial targeting performance and stable fluorescence property, IR780 can penetrate deep into tumor tissues and has been extensively employed in recent studies on mitochondria-targeted therapy.

Ferroptosis is a new type of iron-dependent form of programmed cell death, mainly characterised by mitochondrial swelling, mitochondrial membrane thickening, a reduction in mitochondrial cristae and LPO.[38–40] LPO accumulation (Malondialdehyde) is an important feature of ferroptosis, and GPX4 is a crucial regulatory protein during this process.[41,42] Iron-based nanomaterials are the primary inducers that promote ferroptosis in tumor cells and accumulate within tumor tissues through the targeting and release of iron ions.[36,43,44] The Fenton reaction can occur in the tumor microenvironment to produce a large amount of ·OH radicals for ROS formation and consequently damage the tumor cells. Ferroptosis in tumor cells is promoted by the consumption of intracellular glutathione (GSH) and the increase in LPO levels.[17]

In this work, a fluorescent magnetic nanomaterial Fe_3O_4@DPPC@DMPE-PEG_{2000}-LOD@IR780 (FDLI) with mitochondrial targeting property was designed. Under the action of ACMF, an alternating magnetic thermal effect was generated to increase the local temperature within the tumor tissue, thereby facilitating TMH. Compared with other IR780- or Fe_3O_4-based nanoformulations, FDLI demonstrated enhanced tumor mitochondrial targeting capability, as it was specifically internalized by tumor cells and efficiently transported to the mitochondria, thereby achieving more effective ablation of cancer cells while providing superior protection for surrounding normal tissues. During tumor tissue heating, lactate oxidase (LOD) was released, leading to an increase in H_2O_2 levels. The iron ions then locally exerted enzyme-like activity, damaging the mitochondria and inducing ferroptosis in tumor cells, which resulted in enhanced RT sensitivity. Therefore, the diagnostic performance of FDLI meets the requirements for in vivo multi-modal imaging, enabling precise tumor localisation and targeted drug delivery. Moreover, the mediated magnetic hyperthermia effect,

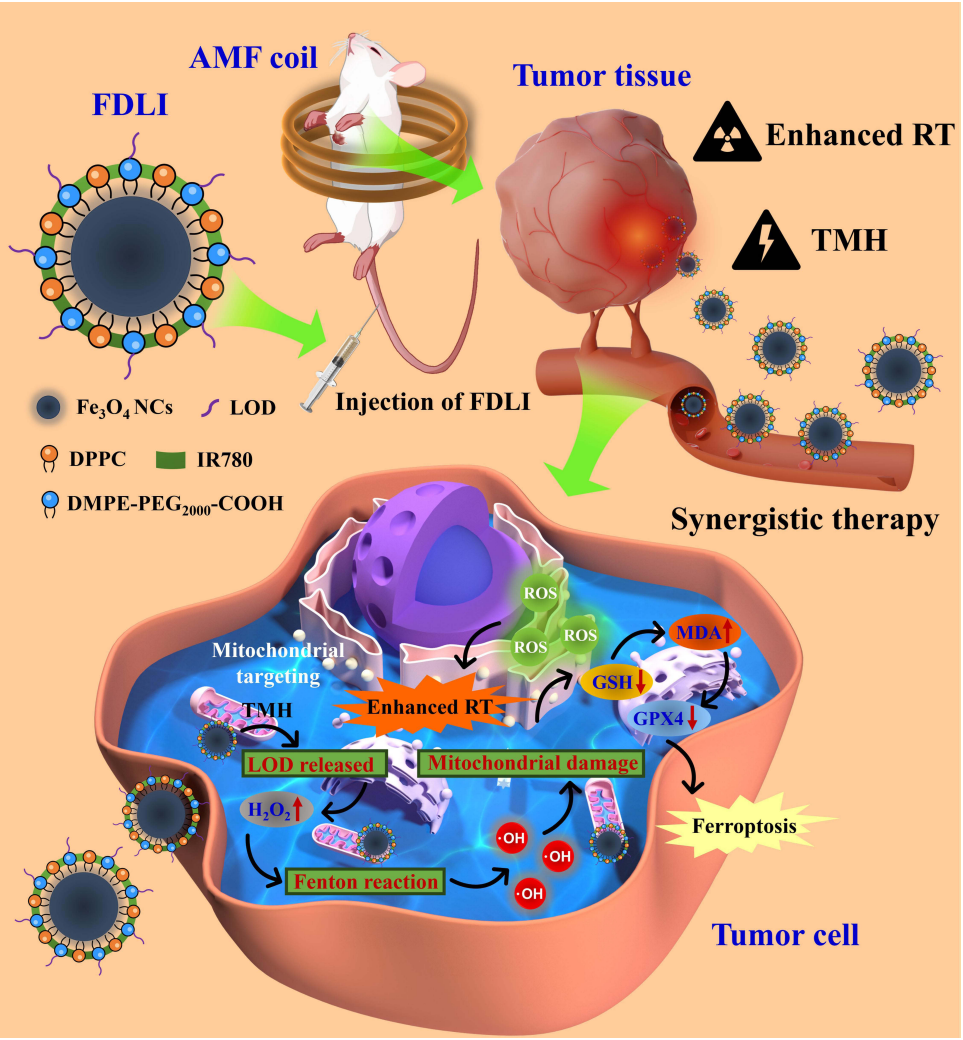

Scheme 1 Schematic representation of the in vivo mechanisms underlying TMH/RT synergistic therapy with FDLI including targeted accumulation in tumor tissues, deep penetration, mitochondrial damage, sustained ROS generation and induced ferroptosis in tumor cells.

enzyme-like activity and RT sensitisation effect contribute to achieving multi-modal tumor treatment, integrating both diagnosis and therapy (Scheme 1).

Materials and Methods

Materials

Iron acetylacetone ($Fe(acac)_3$, 98%), oleic acid (90%), oleylamine (90%), dibenzyl ether (95%), 2-(N-morpholino) ethanesulfonic acid buffer (MES, >99%), 1-ethyl-3-(dimethyl-aminopropyl) carbodiimide hydrochloride (EDC, >99%) and N-hydroxysuccinimide (NHS, >99%) were procured from Shanghai Aladdin Reagent Co., Ltd (China). The phospholipid DPPC (>99%) and DMPE-PEG_{2000}-COOH (>99%) was purchased from Shanghai Ponsure Biotechnology Co., Ltd (China). IR780 (>99%) and LOD (>99%) obtained from Shanghai Yuanye Bio-Technology Co., Ltd (China). The commercially available reagents including iron standard products (≥99%), ethanol (95%) and chloroform (99%) were sourced from Sinopharm Chemical Reagent Co., Ltd (China). Deionized water was produced using an Aquapro Water Purifier (EDI1-1001-U model from Yiyang). All chemicals were employed as received without any additional purification.

https://doi.org/10.2147/IJN.S535222

Preparation of FDLI

In our previous works, a series of magnetic nanomaterials with high-quality characteristics were successfully synthesized.[27,45–47] Based on the prior research foundation, here we further design and synthesize a high-performance magnetic FDLI nanomaterial with mitochondrial targeting function. The detailed preparation methodology is described below. Take 7 g of $Fe(acac)_3$ and measure 100 mL of dibenzyl ether and 23 mL of oleic acid, adding them sequentially to a round-bottom flask. The round-bottom flask is subsequently placed in a high-temperature reactor, where it is heated to 220°C within 1 h and maintained at this temperature for an additional 1 h. Following this, the temperature is raised to 290°C over a period of 21 minutes and held constant for 40 minutes. After cooling to room temperature, the mixture is initially separated through the magnetic attraction and then washed three times with anhydrous ethanol before the addition of 10 mL of chloroform for storage at room temperature, obtaining the High-performance Fe_3O_4 nanocrystals (NCs). Take 40 mg of the prepared Fe_3O_4 NCs, add 240 mg of DPPC and DMPE-PEG_{2000}-COOH in a 1:1 ratio, and also add 2 mg of IR780 probe, 20 mL of chloroform, and 10 mL of deionized water. The mixture was transferred to a round-bottom rotary evaporator, followed by ultrasonication for 15 minutes. Rotary evaporation was then performed at 50–52 °C for 30 minutes to yield water-soluble Fe_3O_4@DPPC@DMPE-PEG_{2000}@IR780 (FDI), which was subsequently stored at room temperature. Prepared FDI was added to 5 mL of 0.02 mol/L MES buffer solution, the pH was adjusted to 5.5, and incubated at 37°C in a dark shaking incubator for 30 minutes. Then, 240 units of LOD, 150 mg of EDC, and 170 mg of NSH were added to the activated FDI solution, the pH was adjusted to 8.4, and incubated at 37°C in a dark shaking incubator for 24 h. Eventually, the FDLI solution was obtained through multiple ultrafiltration centrifugation and purification steps.

Characterization

We weighed different quantities of Fe standard samples (0.25 mg, 0.5 mg, 1 mg, 2 mg, and 4 mg) using a balance, and determined the Fe content of each standard sample using 1,10-Phenanthroline monohydrate spectrophotometry (Shimadzu, UV-2501PC, Japan). We measured the absorbance of the solution at 510 nm on a UV-visible spectrophotometer to create a standard curve. We prepared IR780 solutions in methanol at different concentrations and measured the absorbance of IR780 at 780 nm on a UV-visible spectrophotometer to create a corresponding standard curve. The Fe content of the prepared FDLI was determined by the created standard curve. The morphology of FDLI was examined using transmission electron microscopy (TEM, JEOL, Japan) combined with high-resolution TEM (HRTEM). The samples were diluted in water and dispersed onto amorphous carbon-coated copper grids for TEM analysis. The FDLI were diluted with deionized water and their size was measured using a Malvern particle size analyzer. The chemical structure of IR780 and FDLI samples prepared using potassium bromide pressing method was analyzed in the range of 500–4000 cm^{-1} using a Fourier Transform Infrared Spectrometer (FT-IR, Bruker, Germany) with 1 cm^{-1} spectral resolution. Meanwhile the crystal structure of Fe_3O_4 was also analyzed using Raman spectroscopy (InVia, Renishaw, U.K.). The optical properties and stability of FDLI were evaluated using a UV-Visible spectrophotometer (Shimadzu UV-2501PC, Japan), a fluorescence imaging system (Caliper Life Sciences, USA), and a fluorescence spectrometer (Shimadzu UV-2501PC, Japan). Additionally, the crystal structure of FDLI was characterized using an X-ray diffractometer (XRD, Siemens D-500, Germany). The samples were prepared by dropping a dispersion onto silicon substrates, followed by transferring them into an airtight container to ensure complete evaporation of the solvent. The XRD data were collected in the 2θ range of 5° to 65°at room temperature using Cu Kα radiation on a diffractometer. FDLI exhibits peroxidase-like activity and effectively catalyzes the Fenton reaction, contributing to its potential in oxidative stress-mediated therapeutic applications. In the Fenton reaction system, ferrous ions (Fe^{2+}) react with hydrogen peroxide (H_2O_2) to generate ferric ions (Fe^{3+}), hydroxide ions (OH^-), and hydroxyl radicals (·OH). The corresponding chemical equation is as follows: $Fe^{2+} + H_2O_2 \rightarrow Fe^{3+} + OH^- + \cdot OH$. The ability of FDLI to generate ·OH was evaluated under different temperature and pH conditions using the TMB method in a UV-visible spectrophotometer, with temperature control set at 25°C, 37°C, and 45°C, and pH conditions set at 5.5, 6.5, and 7.5.

Cell Culture

Mouse triple-negative breast cancer (4T1) cells were obtained from the Institute of Cell Science, Chinese Academy of Sciences (Shanghai, China) and cultured in DMEM culture medium containing 10% fetal bovine serum (FBS) and 1% mixture of penicillin-streptomycin antibiotics in a 5% carbon dioxide atmosphere at 37°C.

In vitro CCK-8 Assay

The cell viability was evaluated using the Cell Counting Kit-8 (CCK8) assay to analyze the in vitro cytotoxicity of FDLI. Logarithmic phase 4T1 breast cancer cells were suspended at a concentration of 1×10^5/mL and added to 96-well plates. 100 μL of cell suspension was added to each well. A blank group (without cell suspension or drugs), a control group (without drugs), and experimental groups with different concentrations of FDLI nanoparticles were set up, with three replicate wells in each group. When the 4T1 cells reached a growth density of 70–80%, fresh culture medium was added and the experimental groups were incubated with different concentrations of sterile FDLI dilution solution for 24 h. A CCK8 working solution was prepared at a 1:10 ratio and stored, and the culture medium was removed and the wells were washed with PBS three times. Then, 100 μL of CCK8 working solution was added to each well in the dark and further incubated for additional 1 h prior to measurement. For the control group, we used PBS buffer solution for co-incubation treatment with the cells. The optical density (OD) values of each well in the 96-well plate were detected using a microplate reader at a wavelength of 450 nm. The cell viability was calculated based on these OD values, and the in vitro cytotoxicity of FDLI was quantitatively evaluated by determining the half-maximal inhibitory concentration (IC_{50}).

In vitro Intracellular Imaging

The targeting ability of FDLI towards 4T1 cells and their mitochondria in vitro was evaluated by confocal laser scanning microscopy (CLSM; Leica, DMi8, Germany), while its anti-phagocytosis ability was evaluated in RAW264.7 cells. 4T1 cells and RAW264.7 cells were separately seeded onto sterile coverslips and placed in 12-well plates at a density of 10^6 cells per well. Then FDLI was added, and the cells were incubated at 37°C for 4 h (the final Fe concentration was 50 μg/mL). In the fluorescence targeting and anti-phagocytosis experiment groups, the green mitochondrial fluorescent probe was added and incubated for 20 minutes after which the residual drugs and probe were removed by washing with PBS. DAPI was then added for staining, and the red fluorescence signal was immediately observed using CLSM to observe the degree of overlap between the red fluorescence signal and the green fluorescence signal. In the Prussian blue staining experiment group, FDLI was incubated with the cells for 4 h after which the cells were fixed with 4% formaldehyde for 30 minutes, washed with PBS three times, stained with Prussian blue dye for 30 minutes, washed with PBS three times again, and then stained with 1% nuclear fast red for 30 minutes before being washed with PBS three times again. The results were observed under a microscope.

In vitro Plate Clone Formation Assay

This study used an in vitro plate colony formation assay to evaluate the clonogenic ability and regenerative potential of 4T1 cells under the action of RT with FDLI+ACMF (the final Fe concentration was 100 μg/mL). 4T1 cells were seeded at a proportionate number in 6-well plates and cultured for 24 h. Then, FDLI was added to the cells. After 4 h, the cells were subjected to equivalent magnetic induction hyperthermia, and were treated with different radiation doses (0, 2, 4, 6, and 8 Gy). After radiation, the cells were incubated at 37°C in a 5% CO_2 environment for 10 to 14 days, and then the results were observed using the crystal violet staining method.

Determination of Intracellular GSH Levels in vitro

This study used a GSH quantitative assay kit to determine the GSH content in 4T1 cells. The measured GSH levels were normalized to the protein content of the extracted cells as the standard reference. The specific steps were as follows: First, 4T1 cells were seeded in 6 cm culture dishes and cultured overnight at 37°C, approximately 10^6 cells per dish. Then, the cells were treated with PBS, FDLI, or FDLI + ACMF (the final Fe concentration was 100 μg/mL). According to the

manufacturer's instructions, the GSH level was determined using a UV-visible spectrophotometer (Shimadzu, UV-2501PC, Japan) at a wavelength of 412 nm.

Determination of Intracellular ROS Levels in vitro

This study used the ROS quantitative detection kit to determine the content of ROS in cells. The measured ROS levels were normalized to the protein content of the extracted cells as the standard reference. First, 4T1 cells were seeded in 96-well culture plates at a density of approximately 10^5 cells per well at 37°C overnight. Then, the cells were incubated with Rousp (served as the ROS positive control), PBS, and FDLI, with the drug treatment group incubated for 6 h. It is worth noting that in the FDLI+ACMF group, after adding the drug for 4 h, the cells were subjected to magnetic thermal treatment for 30 minutes at ACMF, and then continued to be incubated in the cell culture incubator for 6 h (the final Fe concentration was 100 μg/mL). The determination of ROS levels was based on the instructions of the above-mentioned kit and conducted using a fluorescence plate reader (BioTek, cooperating with H4, USA) at excitation wavelength of 488 nm and emission wavelength of 525 nm.

In vitro Cell Apoptosis Assay

This study detected cell apoptosis induced by FDLI+ACMF group, FDLI+RT group, and FDLI+ACMF+RT group using Annexin V-FITC/PI fluorescence detection kit. In the apoptosis experiment, flow cytometry was employed for detection, in which we used the Annexin V or PI single staining samples as a single positive control to calibrate the fluorescence compensation parameters. In the assay results, viable cells were defined as Annexin V^-/PI^-, early apoptotic cells as Annexin V^+/PI^-, and both late apoptotic and necrotic cells exhibited the Annexin V^+/PI^+ pattern. A total of 10,000 cells were analyzed in each test. In the figure's quadrant layout, Q2 represents viable cells, whereas Q2 and Q3 collectively indicate apoptotic populations. The specific procedure is described as follows. First, 4T1 cells were seeded in 6-well plates and cultured at 37°C with 5% CO_2 and approximately 10^5 cells per well. The cells were treated according to the experimental conditions, including the PBS group, the single magnetic heating group (ACMF group), the single drug group (FDLI group), the single radiation group (RT group), the FDLI+ACMF combination group, the FDLI+RT combination group, and the FDLI+ACMF+RT combination group. Selectively, X-ray linear accelerator was used at room temperature to irradiate the cells with a dose of 4 Gy (6MV, 500 cGy/min) using the 100 μg/mL Fe as the final concentration. The cells were centrifuged at 1000 rpm and then washed with PBS three times. They were re-suspended in 500 μL of binding buffer. Then, 5 μL of Annexin V-FITC/PI probe was used to label the cells in the dark for 15 minutes. Finally, the fluorescence intensity within the cells was detected using imaging flow cytometry (IFC, Amnis, Flow sight, USA) and analyzed using IDEAS 6.2 software.

In vitro Mitochondrial Membrane Potential Assay

This study used the JC-1 staining kit to assess mitochondrial membrane potential (Ψ_m) and analyzed it using the IFC (Amnis, Flow sight, USA). First, 4T1 cells were seeded in 12-well plates and cultured (37°C, 5% CO_2, approximately 10^4 cells per well). Then, the cells were treated with PBS, single magnetic heat group (ACMF group), single drug group (FDLI group), single radiation group (RT group), FDLI+ACMF combination, FDLI+RT combination, and FDLI+ACMF +RT combination, with the final Fe concentration of 100 μg/mL (12 h, 37°C, 5% CO_2). According to the instructions in the reagent kit, the cells were washed with the prepared 1×JC-1 staining buffer three times after incubation, and then 2 mL of serum-free DMEM medium was added to each well. The content of JC-1 monomer (excitation wavelength 490 nm, emission wavelength 530 nm) and JC-1 polymer (excitation wavelength 525 nm, emission wavelength 590 nm) was detected on a calibrated multi-functional enzyme-linked immunosorbent assay (ELISA) reader. The results have been calibrated for dual fluorescence (monomer vs aggregate) as performed by the ELISA reader.

Mitochondrial TEM Results of 4T1 Cell

The 4T1 cells in the logarithmic phase were suspended and then seeded into 6 cm diameter dishes. When the cells grew to 70%-80% confluency, FDLI (the final Fe concentration was 100 μg/mL) was added, and ACMF treatment was performed for 30 minutes 4 h later. After 24 h, the cells were collected to form a cell suspension, which was centrifuged

at 1200 rpm for 5 minutes, and washed with PBS three times. Then, the cells were fixed with 2.5% glutaraldehyde for 12 h. After centrifugal selection (1000 rpm, 10 min), the cells were collected and stained with 1% uranyl acetate, subsequently dehydrated in a gradient ethanol series (from 25% to 100%), and subsequently embedded in Epon618 resin for TEM (JEOL/JEM-2000E, Japan) observation.

In vitro Cell Cycle Assay

This study evaluated the effects of PBS group, FDLI group, and FDLI + ACMF + RT group on cell cycle using DAPI staining solution. First, 4T1 cells were seeded in 6-well plates (at 37°C, 5% CO2, approximately 10^5 cells per well). The cells were treated with PBS, single drug (FDLI group), or FDLI + ACMF combination (the final Fe concentration was 100 μg/mL) according to the experimental conditions. After 24 h, the cells were collected by centrifugation (1000 rpm), washed with PBS three times, and then suspended in 500 μL DAPI staining solution in the dark for 20 minutes. The fluorescence intensity within the cells was detected using an IFC (Amnis, Flow sight, USA), and the data were analyzed using IDEAS 6.2 software.

In vitro Western Blotting Assay

Western blot (WB) was used to detect proteins related to cell cycle and ferroptosis in tumor cells (Cyclin B1 and GPX4). Specifically, the extracted protein concentration was quantitatively determined using the BCA reagent kit. The proteins were separated by 10% SDS-PAGE and immediately transferred to a PVDF membrane. Next, the membrane was blocked with 5% BSA for 1 h, followed by overnight incubation with specific monoclonal antibodies (anti-Cyclin B1, anti- GPX4 and anti-β-Actin) at 4°C. After washing the membrane with PBST three times, it was incubated with HRP-conjugated rabbit or mouse IgG secondary antibodies (diluted at a ratio of 1:5000, provided by Cell Signaling Technology, Inc., Beverly, MA, USA) at room temperature for 1 h. The signals were detected using the ECL chemiluminescence substrate kit (Pierce Biotechnology, Rockford, IL, USA) and the automatic chemiluminescence imaging system (Amersham Imager 600, provided by General Electric Company, Waltham, MA, USA). Finally, the protein expression was quantitatively analyzed using ImageJ software (version 1.52v, National Institutes of Health, Bethesda, MD, USA).

In vitro Hemolysis Assay

Blood was collected from BALB/c mice into anticoagulant tubes and rinsed repeatedly with PBS until the supernatant became clear. Subsequently, the blood was prepared as a 2% red blood cell (RBC) suspension. Experimental groups included a negative control group (saline), a positive control group (deionized water), and FDLI solutions with varying Fe concentrations. A total of 500 μL of each FDLI solution was transferred into 1.5 mL centrifuge tubes. Then, 500 μL of the RBC suspension was added to each tube, followed by gentle mixing. The mixtures were incubated at 37 °C for 12 h. Finally, images of the RBC suspensions and drug mixtures were captured for documentation.

Animal Protocol

6–8 week-old BALB/c female mice were purchased from Changzhou Caveness Co. and were housed in a specific pathogen-free laboratory. 4T1 cells in the logarithmic growth phase were collected, digested, and suspended in PBS. The cells were centrifuged at 1000 rpm for 3 minutes, and then re-suspended in PBS to achieve a cell concentration of 1×10^8 cells/mL. 200 μL of the cell suspension was injected into the right breast subcutaneously of BALB/c mice using a 1 mL insulin syringe. Once the tumors grew for about a week (volume approximately 50–70 mm^3), a successful in vivo mammary in situ subcutaneous tumor model was established. All animal care and experimental procedures were conducted in accordance with the "Rules and Guidelines for Animal Management of the Ministry of Health, People's Republic of China" and approved by the Animal Ethics Committee of Xuzhou Medical University and Jiangsu Normal University, with ethics approval number JSNU-IACUC-2024040.

BALB/C mice bearing tumors were randomly divided into seven groups: (1) Control Saline group; (2) Single ACMF group; (3) Single FDLI group; (4) Single RT group; (5) FDLI + ACMF combination group; (6) FDLI + RT combination group; (7) FDLI + ACMF + RT combination group. On the first day, each mouse received an intravenous injection via the tail vein of either saline (200 μL per mouse) or FDLI (20 mg/kg, 200 μL per mouse). On the second day, ACMF treatment was administered at a frequency of 390 kHz and a magnetic field strength of 2.58 kA m^{-1} for 30 minutes. On

the third day, radiation therapy was delivered using a 6 MV X-ray linear accelerator at a dose of 1000 cGy. ACMF treatment was repeated on the fifth and seventh days under the same conditions (390 kHz, 2.58 kA m^{-1}, 30 minutes). No treatment was given on the fourth, sixth, and eighth days, completing the first treatment cycle. The second treatment cycle was conducted from the ninth to the sixteenth day, following the same protocol as the first cycle.

In vivo Fluorescence Imaging

Select BALB/c mice with established breast cancer models, and inject FDLI (20 mg/kg, 200 μL per mouse) via the tail vein. Set up a small animal fluorescence imaging instrument with an excitation wavelength of 740 nm and an emission wavelength of 820 nm to monitor the fluorescence signals of mice before and after 4 h, 12 h, 24 h, 36 h, 48 h, 60 h, 72 h, 96 h, and 120 h of drug administration. Use Living Image software to process the data and extract the fluorescence signal strength of the tumor local (I_T) and adjacent tissue (I_M), calculate the CI value (I_T/I_M) to evaluate the targeting effect of FDLI in live tumors in mice.

In vivo MR Imaging

The in vivo MRI experiments of FDLI under selective ACMF were carried out under a 38 mm circular animal coil on a 7.0 T Micro-MRI (PharmaScan, Brukers, Germany). In situ T2-MRI scanning tests of tumor-bearing mice were performed at an appropriate time prior and post tail vein injection of FDLI, and the injection dose was 20 mg Fe per kg body weight. In the first place, tumor-bearing mice are anesthetized by breathing isoflurane (1.5%) through the nasal cavity, and then maintain their body temperature at about 37°C. The cross-sectional scan was utilized to observe the imaging of the tumor site in mice.

In vivo Heat Imaging

Select BALB/c mice with established breast cancer models and inject FDLI via the tail vein. 24 h later, perform ACMF treatment on the mice and monitor the local temperature changes of the tumors using a thermal imaging device, while taking relevant images.

Histological Examination

On day 16, mice with 4T1 tumors in different groups were euthanized, the major organs or tissues were excised, and fixed with 4% paraformaldehyde, then embedded in 3–5 mm thick paraffin. In the histological analysis, the tissue sections were dewaxed with xylene, stained with hematoxylin and eosin (H&E) dye and sealed with neutral glue for optical microscope observation. In the immunohistochemistry (IHC) staining process, the tumor paraffin sections were dewaxed and rehydrated before extracting the antigen. Then, the sections were treated with a 3% hydrogen peroxide solution for 10 minutes to block endogenous peroxidase activity, followed by a 1-h incubation with 5% BSA to block non-specific binding, and digest proteins with Proteinase K. The sections were washed with PBS three times, then incubated with primary antibodies (CD31(diluted at a ratio of 1:20), Ki-67 (diluted at a ratio of 1:200), and HIF-1α diluted at a ratio of 1:50)) at 4°C overnight. After that, the sections were incubated with HRP-conjugated goat anti-rabbit secondary antibody (diluted at a ratio of 1:200) for 20 minutes. After adding the DAB chromogen solution, the sections were incubated with hematoxylin dye solution for 5 minutes, then sealed with neutral glue and observed under an optical microscope.

In the Masson and TUNEL staining process, the tumor paraffin sections were dewaxed and rehydrated, then stained with hematoxylin for 5 minutes. After three washes with distilled water, the sections were stained with Masson and TUNEL staining reagents according to the instructions for optical microscopy observation. In the Prussian blue staining, the mouse tumor tissue sections were hydrated and immersed in the potassium ferrocyanide-hydrochloric acid solution for 30 minutes, followed by PBS washing. Then the nucleus was stained with nuclear fast red dye for 30 minutes, followed by a 10-minute wash with PBS. Finally, the sections were mounted and observed under the microscope and relevant images were captured.

In vivo Western Blotting Assay

WB was used here to detect proteins related to apoptosis and ferroptosis in tumor tissues (Bax, Bcl-2, γ-H2A.X and GPX4). Specifically, the tumor tissues were homogenized on ice with RIPA buffer for 30 minutes, and centrifuged at 12,000 rpm for 10 minutes to obtain the supernatant. Then, the extracted protein concentration was quantitatively determined using the BCA reagent kit. The proteins were separated by 10% SDS-PAGE and immediately transferred to a PVDF membrane. Next, the membrane was blocked with 5% BSA for 1 h, followed by overnight incubation with specific monoclonal antibodies (anti-Bax, anti-Bcl-2, anti-γ-H2A.X, anti-GPX4 and anti-β-Actin) at 4°C. After washing the membrane with PBST three times, it was incubated with HRP-conjugated rabbit or mouse IgG secondary antibodies (diluted at a ratio of 1:5000, provided by Cell Signaling Technology, Inc., Beverly, MA, USA) at room temperature for 1 h. The signals were detected using the ECL chemiluminescence substrate kit (Pierce Biotechnology, Rockford, IL, USA) and the automatic chemiluminescence imaging system (Amersham Imager 600, provided by General Electric Company, Waltham, MA, USA). Finally, the protein expression was quantitatively analyzed using ImageJ software (version 1.52v, National Institutes of Health, Bethesda, MD, USA).

Hematologic Examination

On day 16, the whole blood of 4T1 tumor-bearing mice was collected for liver and kidney function tests and routine blood tests. All hematological tests were provided by the Department of Clinical Laboratory Medicine of Xuzhou Central Hospital.

In vivo Anti-Tumor Efficacy Evaluation

The in vivo anti-tumor efficacy of the compound was assessed by analyzing tumor volume, body weight changes, and survival rate 16 days post-treatment. Mouse body weight was monitored every other day throughout the 16-day observation period. Furthermore, at the conclusion of the treatment regimen, the survival duration and survival rate were evaluated across different experimental groups. Following completion of two treatment cycles, mice were permitted to survive until the end of the designated survival period, after which they were euthanized for histopathological examination. Lung tissue was excised ex vivo for observation and imaging analysis to evaluate potential liver and lung metastasis.

Results and Discussion

Evaluation of Physicochemical Properties

TEM result revealed that FDLI exhibited a core-shell structure after negative staining with phosphotungstic acid. The core was composed of uniform, sphere-like magnetic nanoparticles with a particle size of 18–23 nm, while the shell appeared as a single-layer white halo containing a uniform and dense phospholipid monolayer, indicative of good single dispersion (Figure 1A). Based on the results, the hydrodynamic size of FDLI was approximately 120 nm with a uniform distribution, indicating good colloidal stability (Figure 1B). FTIR analysis demonstrated the characteristic peaks of IR780, including stretching and bending vibration of C-Cl, within 850–600 cm^{-1}. The characteristic peaks of carbon chain, including v(C-C), v(C=C) and v(C≡C) respectively at 1320,1450 and 2350 cm^{-1}, and amide bonds, including v (O-H) and v(N-H), appeared at 3500–3100 cm^{-1}, demonstrating that LOD is covalently linked to the FDI surface (Figure 1C). Raman spectra demonstrated that the lattice vibration peaks of multiple iron ions and the bending and stretching vibration peaks of Fe–O were detected around 230, 295, 410, 520 and 665 cm^{-1}, corresponding to the characteristic Raman peaks of Fe_3O_4. The ligand IR780, primary composed of a benzene ring, showed characteristic peaks between 990 cm^{-1} and 1600 cm^{-1} (Figure 1D). The crystal structure of FDLI was examined using XRD, and the result is shown in Figure 1E. FDLI showed the characteristic diffraction peaks of Fe_3O_4 at 18.333°, 30.157°, 35.521°, 37.157°, 43.172°, 53.561°, 57.098° and 62.703° corresponding to the (111), (220), (311), (222), (422), (511) and (440) crystal planes, respectively (Figure 1E). This finding indicates that the crystal structure and main chemical composition of FDLI can be determined as the inverse spinel cubic structure of Fe_3O_4 NCs.

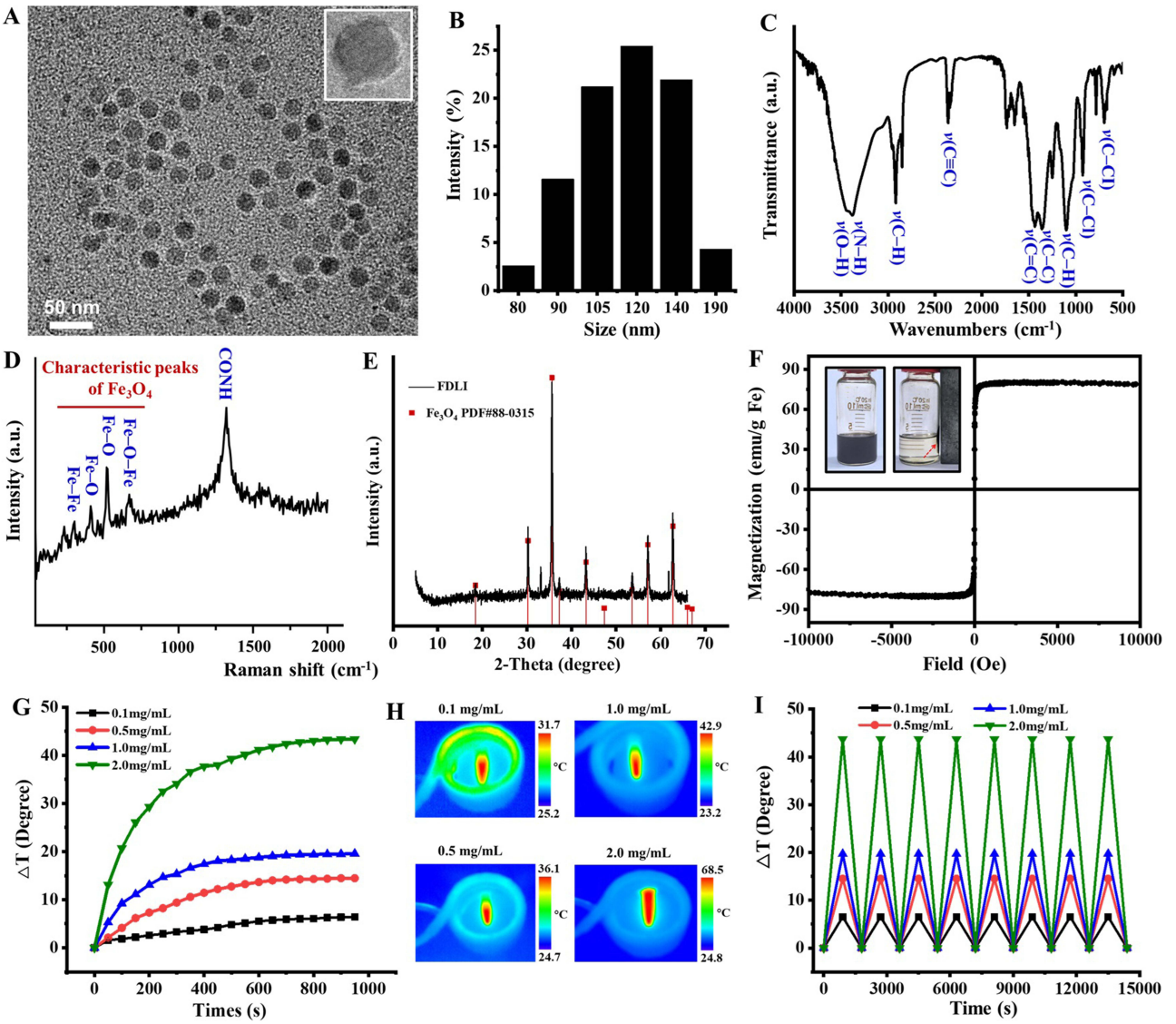

Figure 1 (**A**) TEM image of FDLI. (**B**) The hydrodynamic size of FDLI. (**C**) Infrared spectroscopy of IR780 and FDLI. (**D**) Raman spectra of FDLI. (**E**) The crystal structure of FDLI. (**F**) VSM results of FDLI, the inset showed the digital images of samples. The red arrows indicate the adsorbed Fe_3O_4 NPs. (**G**) The heating performance and heating rate of FDLI with different concentration (0.1mg, 0.5mg, 1.0mg, 2.0mg of Fe/mL over 950s). (**H**) The thermal image of FDLI with an ACMF action. (**I**) Heating stability performance of FDLI.

High magnetic and magnetothermal properties are key indicators for evaluating the high performance of FDLI. VSM results showed that the coercivity and remanence of FDLI are approximately zero, demonstrating its strong super-paramagnetic property (Figure 1F). FDLI also presented excellent heating performance in an alternating magnetic field, and its heating rate rapidly accelerated with its concentration. At 2 mg of Fe/mL, the temperature reached approximately 68°C and the SAR was calculated as 324 W/g Fe (Figure 1G and H), showing a good magnetothermal effect. After multiple magnetic induction hyperthermia treatments, FDLI exhibited stability at high temperatures, implying excellent heating stability performance (Figure 1I).

The UV absorption and fluorescence spectra of FDLI were measured to evaluate its optical property. The results showed that FDLI has a distinct UV absorption peak within the range of 760–820 nm, with the maximum absorption peak around 800 nm, characteristic of IR780. When the excitation wavelength is 745 nm, FDLI exhibits a maximum emission peak at 835 nm (IR780 has fluorescent properties), reaching the near-infrared region, thus meeting the criteria for in vivo diagnosis (Figure 2A). The fluorescence intensity of FDLI was continuously monitored for 1 month to verify its

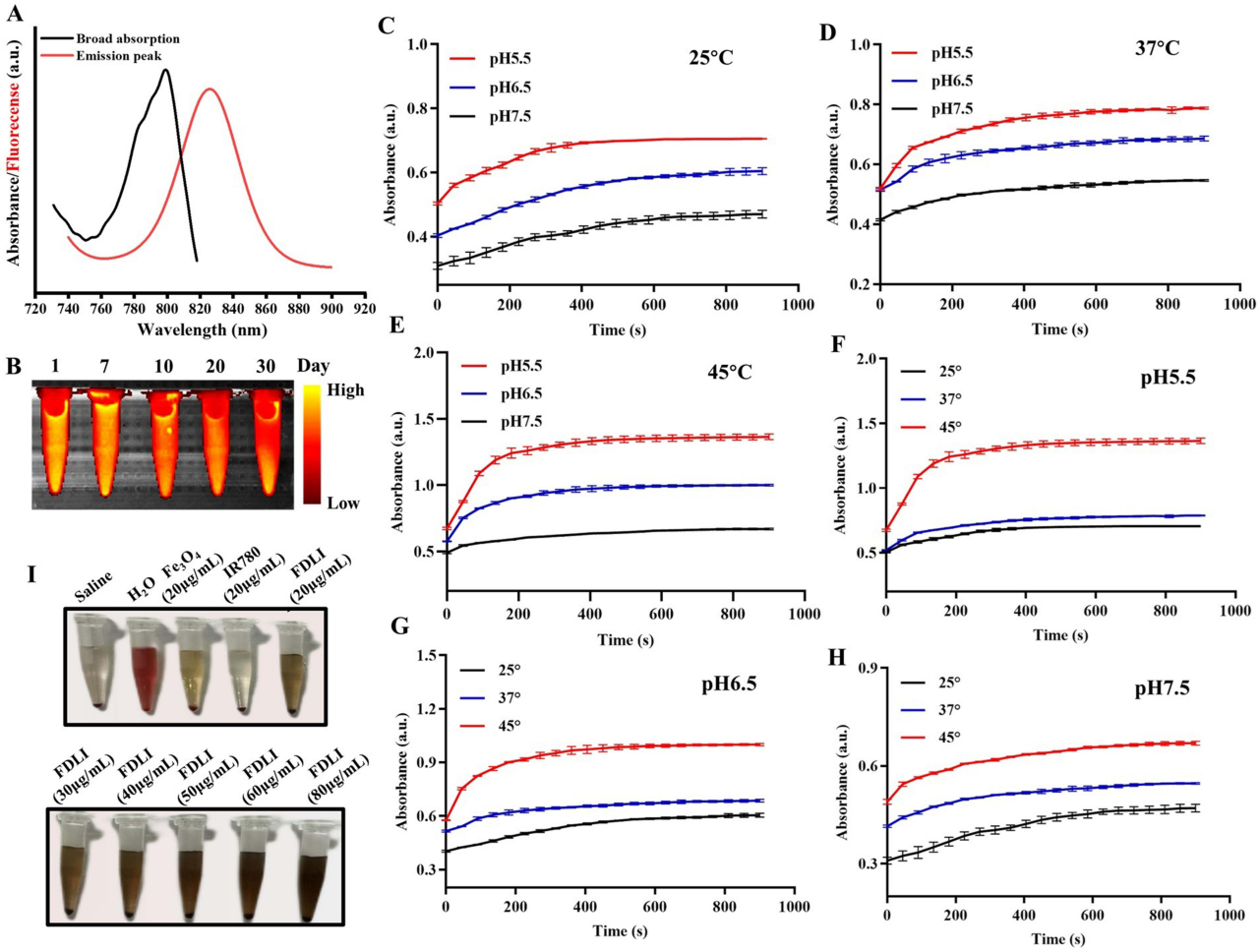

Figure 2 (**A** and **B**) The UV absorption and fluorescence spectra of FDLI (E_x: 745 nm; E_m: 820 nm). (**B**) The fluorescence stability of FDLI in 1 month. (**C–H**) The peroxidase-like activity of FDLI under different pH levels (5.5, 6.5 and 7.4) and temperatures (25°C, 35°C and 45°C). (**I**) The haemolysis assay of saline, H_2O, Fe_3O_4, IR780 and FDLI (20μg, 30μg, 40μg, 50μg, 60μg and 80μg Fe per mL).

fluorescence stability, and no significant change in fluorescence intensity was observed during this period, indicating that FDLI possesses an outstanding fluorescence property and photobleaching resistance (Figure 2B).

Evaluation of Peroxidase-Like Activity

Magnetic nanoparticles can exhibit peroxidase-like activity in the mildly acidic microenvironment of tumors (Fenton reaction). Highly toxic ·OH are generated by catalysing endogenous H_2O_2, which is the basis of their function in the chemokinetic therapy of tumors. In this study, the in vitro peroxidase-like activity of FDLI was evaluated under different pH levels (5.5, 6.5 and 7.4) and temperatures (25°C, 35°C and 45°C) and the tetramethylbenzidine (TMB) method was adopted to measure ·OH generation. TMB can be dissolved in water to form a colourless liquid; when ·OH is produced, it can be combined with the TMB probe to form a blue precipitate, showing a characteristic absorption peak at 641 nm. The ability of FDLI to catalyse H_2O_2 for ·OH generation can be indirectly evaluated by detecting the intensity of the absorption peak at this wavelength. The results showed that with the increase in acidity and temperature, the amount of ·OH produced by catalysis gradually increased, indicating that FDLI can effectively exert its peroxidase-like activity in acidic and hyperthermic environments (Figure 2C–H).

For the in vivo administration of FDLI, the haemolysis assay was conducted to evaluate the biocompatibility of FDLI with red blood cells. Different concentrations of FDLI (20, 30, 40, 50, 60 and 80 μg/mL) were exposed to a suspension of red blood cells and then compared with the negative (saline) and positive (H_2O) control groups to verify the biological

https://doi.org/10.2147/IJN.S535222

safety of FDLI (Figure 2I). The results showed that when the Fe concentration of FDLI was below 70 μg/mL, the red blood cells settled at the bottom of the EP tubes, with the supernatant maintaining a clear boundary between the sedimented cells and liquid. This lack of haemolysis indicates that FDLI possesses good biological safety.

Evaluation of in vitro Cytotoxicity

We first examined the effect of FDLI on cell viability in vitro. Specifically, the CCK8 assay was used to investigate the toxicity effects of different FDLI concentrations on 4T1 cells (Figure 3A). When incubated with FDLI at a low concentration (0–60 μg Fe/mL), the cell survival rate was maintained above 80%. This could be attributed to the enhanced biocompatibility of FDLI after a phospholipid layer is formed on the nanoparticle surface, which can effectively reduce cytotoxicity. Further increase in its dosage (above 100 μg of Fe/mL) revealed the concentration-dependent cytotoxicity of FDLI, with a cell survival rate of only 47%.

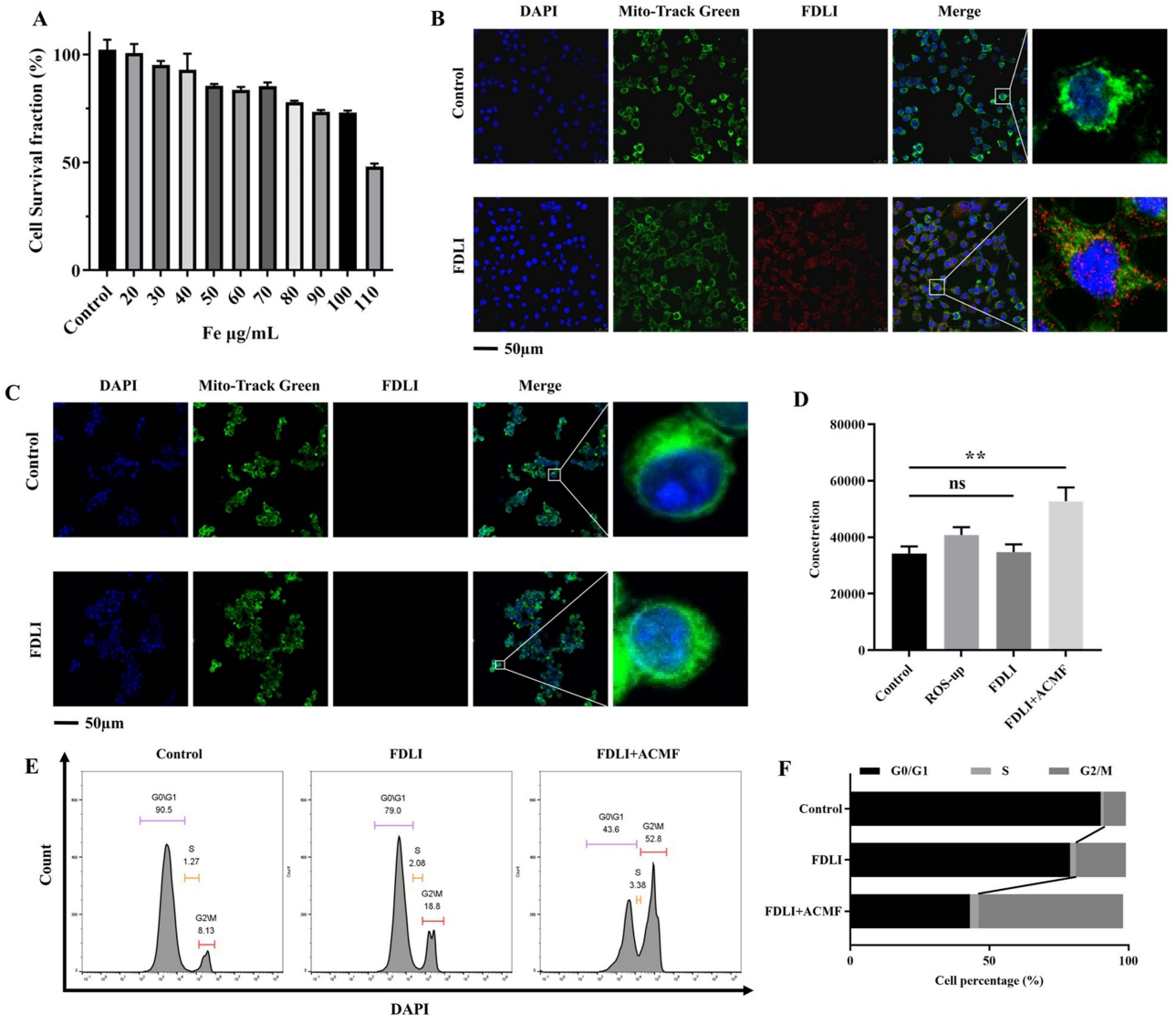

Figure 3 (**A**) Cytotoxicity of 4T1 cells after treatment with FDLI at different concentrations for 24 h. (**B** and **C**) Fluorescence imaging of 4T1 cells after 4-h incubation with FDLI (red-staining) and Fe3O4@DPPC. Cell nuclear staining (blue) and mitochondria-targeted probe staining (green) were visible in all the groups. (**D**) The intracellular ROS production level was measured using microplate reader. (**E** and **F**) The analysis of cell cycle distribution of 4T1 cells treated with FDLI before and after ACMF exposure by flow cytometry (ns: $p>0.05$, **$p<0.01$).

Evaluation of in vitro Cellular Targeting Ability

IR780 is a fluorescent probe with a strong ability to target cellular mitochondria. Here, the ability of FDLI to target tumor cellular mitochondria was assessed via fluorescent label co-localisation under a confocal fluorescence microscope (Figure 3B). Only nuclear staining (blue) and mitochondria-targeted probe staining (green) were visible in the control group. By contrast, the FDLI-incubation group exhibited intense red fluorescence in the tumor cytoplasm and the red signal overlapped with the green fluorescence signal area of the mitochondrial targeting probe, indicating FDLI's good mitochondrial targeting ability.

Macrophages are the main component of the immune system in organisms and have various biological functions, including phagocytosis, killing, antigen presentation and immune regulation. The RAW264.7 mouse monocyte macrophage cell line was utilised in vitro to simulate the in vivo immune response at the cellular level and evaluate the long-circulating ability of FDLI. Specifically, FDLI and RAW264.7 macrophages were incubated for 12 h, and the fluorescence signals were detected under a confocal microscope. The results showed no significant red fluorescence signal in the FDLI-treated RAW264.7 macrophage group, suggesting no evident FDLI phagocytosis. This finding demonstrates that FDLI has good anti-phagocytosis property and long circulation ability (Figure 3C).

Evaluation of in vitro Cellular ROS Levels

The DCFH-DA fluorescent probe can deeply penetrate cell membranes, where it is deacetylated by esterase into nonfluorescent compounds and then oxidised by ROS to generate DCF. Using this probe, the intracellular ROS production level was measured using flow cytometry and a microplate reader (Figure 3D). Compared with the control group, the intracellular ROS level slightly increased after the interaction between FDLI and 4T1 cells. The FDLI-incubated cell culture dish was placed in the ACMF coil for the magnetic induction heating experiment to evaluate the influence of ACMF on intracellular ROS production (magnetic field strength, frequency: 390 kHz and 2.58 kA m^{-1}). After subjecting the cells to magnetic induction heating, intracellular ROS levels were further enhanced. This finding implies that the iron ions in high-concentration FDLI exert an enzyme-like activity to increase the intracellular ROS levels and enhance cytotoxicity.

Evaluation of in vitro Cell Cycle

Tumor cells in the G2/M phase are highly sensitive to radiation, and hyperthermia can effectively arrest the cell cycle in the G2/M phase. Flow cytometry was utilised to analyse and quantify the cell cycle distribution of 4T1 cells treated with FDLI before and after ACMF exposure (Figure 3E and F). The results showed that after different treatments, the cell cycle was affected by FDLI and the mediated magnetothermal effect. In particular, the G2/M phase was remarkably increased after treatment with FDLI plus ACMF, confirming that hyperthermia effectively arrests the tumor cell cycle in the G2/M phase. Furthermore, the characteristic protein cyclin B1 was quantitatively detected using WB (Figure 4A). Cyclin B1 is the key rate-limiting factor regulating the transition from the G2 phase to the M phase of the cell cycle. It forms the M-phase promoting factor (MPF) complex by binding to the cell cycle-dependent kinase CDK1, thereby driving the cell into the mitotic stage. Unprocessed and completed WB results of GADPH and Cyclin B1 were shown in Figures S1 and S2.

Its expression was higher in the control and FDLI-treated groups but significantly decreased after treatment with FDLI plus ACMF. These results further support the conclusion that the combined effect of FDLI and ACMF can effectively arrest the cells in the G2/M phase, providing a theoretical basis for RT sensitisation.

Evaluation of in vitro Cell Apoptosis

Cell apoptosis is one of the major mechanisms of programmed cell death induced by anti-tumor therapies. Cell membranes and nuclei were labelled by FITC-annexin V/PI dual staining, and the apoptotic cells were assessed using flow cytometry to calculate the proportion of cells in each phase of apoptosis (Figure 4B). After treatment with FDLI plus ACMF, the cell apoptosis rate reached 66.1%. By contrast, the cell apoptosis rate reached 64.2% after treatment with FDLI plus RT. The RT here was performed at a dose of 2 Gy (6MV, 500 cGy/min) using an X-ray linear accelerator. The apoptosis rates of these two groups were significantly improved and higher than those of the control (apoptosis rate: 2.1%), FDLI-treated (apoptosis rate:

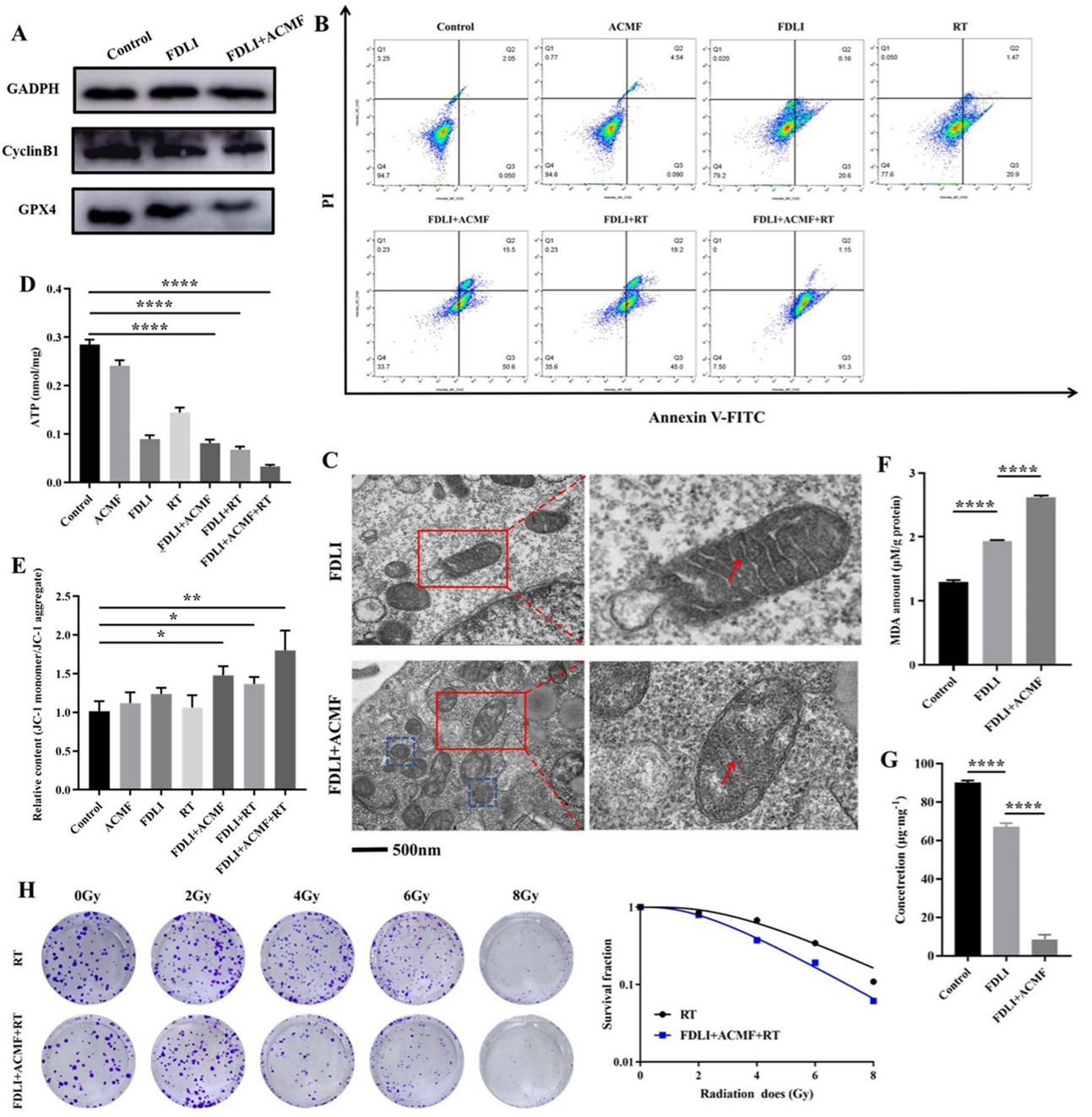

Figure 4 (**A**) Western blotting of Cyclin B1 and GPX4 in vitro 4T1 cells. (**B**) Cell apoptosis was assessed using flow cytometry to calculate the proportion of cells in each phase of apoptosis. (**C**) The damage to cellular mitochondria after treatment with FDLI plus ACMF by examining the ultrastructure of cells. (**D**) Compared with the control and other groups' ATP content. (**E**) mitochondria damage in 4T1 cells labeled with JC-1 dye as an indicator using a microplate reader compared with the control and other groups. (**F** and **G**) MDA and GSH levels of control, FDLI and FDLI+ACMF. (**H**) Colony formation experiment of 4T1 cells treated with Saline and FDLI+ACMF under 2, 4, 6 and 8 Gy radiation, SER is 1.5 (*p<0.05, **p<0.01, ****p<0.0001).

20.22%), RT-treated (apoptosis rate: 22.37%) and ACMF-treated (apoptosis rate: 4.3%) groups. After treatment with FDLI plus ACMF and RT, the apoptosis rate reached 92.45%. This finding suggests that the magnetic induction heating effect of FDLI, in synergy with RT, enhances anti-tumor activity and promotes cell apoptosis.

Evaluation of Mitochondrial Function

Mitochondria are the main organelles where intracellular tricarboxylic acid cycle and oxidative respiratory chain occur. Their primary functions include oxidative energy supply, metabolic regulation, protein synthesis, cellular function maintenance and energy metabolism. First, we visually evaluated the damage to cellular mitochondria after treatment with FDLI plus ACMF by examining their ultrastructure (Figure 4C). The results showed that the structure of the normal mitochondria was mainly composed of the outer membrane, inner membrane, matrix and intermembrane space, with the inner membrane folding inwards to form the mitochondrial cristae. After the treatment, the mitochondrial cristae were significantly reduced and the mitochondrial membrane was thickened, indicating that the mitochondrial structure was damaged. Noticeable injury to the endoplasmic reticulum was also observed and associated with the interaction between mitochondria and endoplasmic reticulum, which also affects the Ca^{2+} content in tumor cells. These damages led to tumor cell death.

Adenosine triphosphate (ATP) is the main energy source for the body, and mitochondria are the main site of ATP production. Accordingly, the cellular mitochondrial function was evaluated by measuring the intracellular ATP content (Figure 4D). Compared with the control and other groups, the ATP was the lowest in the cells treated with FDLI plus ACMF and RT. Moreover, to verify the relationship between apoptosis and mitochondria damage, we used a JC-1 kit to measure the mitochondrial membrane potential changes in 4T1 cells using a microplate reader (Figure 4E). The JC-1 probe can selectively enter mitochondria, and its color changes from orange to green, indicating a decrease in mitochondrial membrane potential. Under membrane polarization conditions, its emission wavelength shifts from 590 nm (JC-1 aggregates, normal state) to 530 nm (JC-1 monomers, damaged state). We measured the absorbance values at these two selected wavelengths and calculated the ratio of JC-1 monomers to JC-1 aggregates to evaluate the degree of intracellular mitochondrial structural damage. A higher ratio indicates more severe mitochondrial damage. Among all groups, the group treated with FDLI plus ACMF and RT showed the highest signal value of the monomeric form of JC-1 probe in cells. This finding indicates that the synergistic effect of inducing pro-apoptotic activity through the intrinsic mitochondrial pathway is achieved, which is consistent with the results of the aforementioned intracellular ATP detection.

Evaluation of Lipid Peroxidation Effect

Lipid peroxidation refers to the process in which lipid substances are oxidised by strong oxidising agents, leading to peroxide formation. During this process, the fluidity and permeability of cell membranes can be changed and the DNA and proteins of cells are damaged, thus affecting normal cellular function. We used a lipid peroxidation assay kit to quantitatively measure malondialdehyde (MDA) levels in tumor cells after various treatments, utilising a microplate reader (Figure 4F). The group treated with FDLI plus ACMF and RT exhibited the highest MDA level, indicating that the combined effect can significantly enhance cellular MDA levels, satisfying the prerequisite for subsequent RT sensitisation. GSH is one of the main antioxidants in the body; it has an integrated detoxification function and can scavenge free radicals in the body. The degree of lipid peroxidation was indirectly evaluated by detecting intracellular GSH levels (Figure 4G). The results showed that the group treated with FDLI plus ACMF and RT exhibited the lowest GSH level, indicating a reduced free radical scavenging ability of the cells, which leads to increased cell damage. The resistance of 4T1 to ionising radiation was also reduced, which is one of the routes to enhance RT sensitivity. Ferroptosis is a regulated form of cell death triggered by lipid peroxidation. GPX4 serves as a core regulatory factor in ferroptosis, and it inhibits the process by specifically catalyzing the reduction of intracellular lipid peroxides to non-toxic lipid alcohols through a glutathione-dependent mechanism.

Based on the above WB results (Figures 4A and S3), it is evident that under the regulation of ACMF, FDLI induces GSH depletion, disrupts mitochondrial structure, and promotes lipid peroxidation, leading to elevated MDA levels and a more pronounced inhibitory effect on GPX4. These findings further demonstrate that the combined application effectively promotes ferroptosis in tumor cells.

Evaluation of Radiotherapy Sensitisation Effect

The colony formation assay is one of the most effective methods for assessing cell proliferation ability. A colony formation experiment was conducted to further verify the RT sensitisation effect of FDLI and its mediated magnetothermal effect on tumor cells (Figure 4H). The results demonstrated that as the radiation dose increased, the survival fraction of the cells in each group gradually decreased. Compared with RT alone, FDLI plus ACMF significantly inhibited cell proliferation. Using the multi-target single-hit mathematical model, the sensitisation enhancement ratio of the combination group was calculated as 1.654, confirming that FDLI and its mediated magnetic hyperthermia exhibit great potential as radiosensitisers.

Evaluation of in vivo Enrichment Effect

A mouse model of subcutaneous breast cancer tumor was established to verify FDLI enrichment in tumors in vivo. Following tail vein injection (dose: Fe 20 mg/kg), an in vivo fluorescence imaging system was used to dynamically monitor fluorescence intensity in the whole body and tumor regions of the mice before and 0.5 h after treatment for 5 days (Figure 5A). The results showed that within 0.5 h after administration, the fluorescence signal was distributed and enriched throughout the mouse body. Over time, the fluorescent signal began to concentrate in the mouse tumor area, reaching the highest concentration in the tumor tissue at 48 h. Meanwhile, the intensity of the fluorescence signal in the target area was higher than that in the surrounding normal tissues, indicating that FDLI has a significant active targeting effect. Statistical analysis of the fluorescence signal ratio between the tumor region and surrounding tissues (ie CI value) was conducted to quantitatively evaluate the intensity of fluorescence signals. At 48 h post-administration, the CI was 3.84, indicating a significant fluorescence contrast effect (Figure 5B). Observation after the staining of isolated tissue sections revealed the presence of numerous FDLI in the tumor tissue and a small amount in the liver and spleen (Figure 5C). As a potential magnetic resonance (MR) contrast agent, FDLI exhibit significant T2-weighted imaging capabilities. To evaluate their performance, FDLI were administered intravenously in a mouse subcutaneous breast

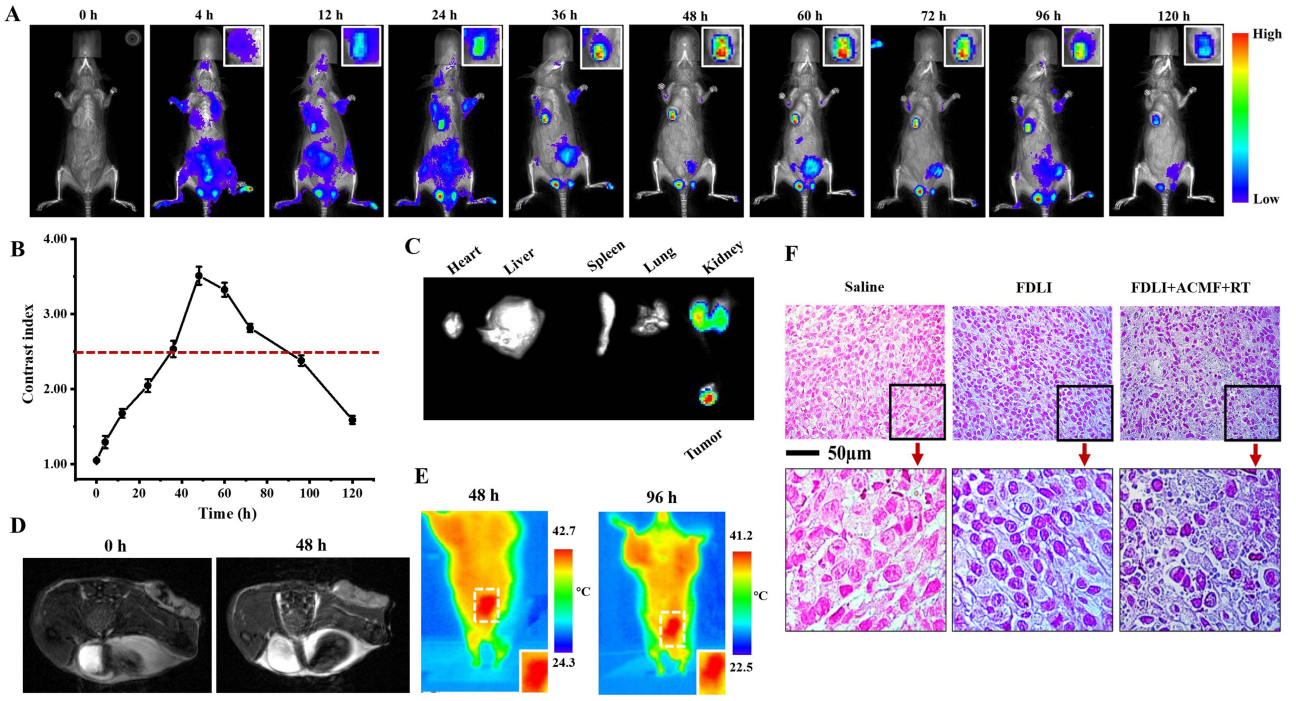

Figure 5 (**A**) Biodistribution of FDLI monitored and quantified by in vivo fluorescence imaging (0~120 h, injection dose: 20 mg/kg body weight, 200 μL per mouse). (**B**) The corresponding fluorescence signal-based CI values changing at tumor sites at different post-injection times (0~120 h). (**C**) Ex vivo fluorescence images of heart, liver, spleen, lung, kidney and tumor collected at 48 h post-injection point. (**D**) In vivo T2-weighted real-time MRI of tumor region in mice before and after i.v. injection FDLI at 48 h post-injection point. (**E**) Thermal images of tumor surface in mice on the 1st and 5th days after TMH treatment, respectively. (**F**) Tumor tissue sections' dual staining (nuclear fast red for nuclei and prussian blue for magnetic nanoparticles).

cancer solid tumor model, and the enrichment of FDLI in the tumor region over a 48-h period was monitored using magnetic resonance imaging (Figure 5D). The results demonstrated that prior to administration, the tumor regions of the mice exhibited high signal intensity (bright areas) in the MR images. Following intravenous injection, FDLI gradually accumulated in the tumor region, leading to a progressive reduction in T2-weighted signal intensity, which appeared as "dark" hole-like signal spots at 48 h post-administration. These findings suggest that the PEGylation of the lipid outer layer of FDLI effectively reduces clearance by the immune system and reticuloendothelial system, thereby enhancing their long-circulation properties in vivo. Additionally, the IR780 ligands on the surface of FDLI further improve targeting specificity for tumor tissues, significantly increasing both the accumulation and retention time of FDLI within the tumor. The tumor region in mice was subjected to magnetic hyperthermia using ACMF (frequency of 390 kHz and magnetic field strength of 2.58 kA/m), and an infrared thermal imaging system was employed to monitor real-time temperature changes on the tumor surface, providing timely feedback on the therapeutic effects. After a single administration of magnetic induction hyperthermia to the tumor, the temperature on the tumor surface was increased (the highest temperatures on the tumor surface reached 42.7°C and 41.2°C at the 48h and 96h after hyperthermia treatment, respectively); all these temperatures met the requirements for effective hyperthermia (Figure 5E). To precisely assess the localisation of FDLI in tumor tissue, we removed the tumor tissues from the mice after intravenous injection, prepared tissue sections and performed dual staining (nuclear fast red for nuclei and Prussian blue for magnetic nanoparticles). These sections were observed under an optical microscope to determine the distribution of magnetic nanocrystals. The results showed that FDLI was enriched in the tumor cells of mice after administration (indicated by the blue signal), and the enrichment level was further increased after magnetic hyperthermia treatment (Figure 5F). This finding suggests that the heat generated during hyperthermia destroyed the structure of the tumor's new blood vessels, causing them to dilate under high temperatures and significantly enhancing their permeability and infiltration. This phenomenon allows FDLI to easily penetrate the tumor tissue through the "gaps" on the surface of new blood vessels to promote its accumulation in the target area.

Evaluation of in vivo Anti-Tumor Therapeutic Effects

Imaging technology was employed for tracking and targeted imaging of FDLI in the tumors for in situ monitoring, providing detailed and accurate diagnostic information for subsequent tumor treatment. In practice, a single dose of FDLI injected into mice is insufficient to achieve effective TMH and RT at the tumor site. To allow FDLI to fully accumulate within the tumor tissue and obtain sufficient therapeutic effects, we designed two diagnosis and treatment cycles (16 days), including two intravenous injections (FDLI with a dose of Fe 20 mg/kg was administered via the tail vein on the 1st and 8th days after tumor establishment). TMH was conducted on the 2nd, 3rd, 4th, 9th, 10th and 11th days (magnetic field strength, frequency: 390 kHz and 2.58 kA m^{-1}), and RT was performed on the 3rd and 10th days (The RT here was performed at a dose of 5 Gy (6MV, 1000 cGy/min) using an X-ray linear accelerator). The mice were randomly divided into seven groups: (1) tail vein injection of normal saline (saline) as the control group; (2) ACMF-treated group; (3) tail vein injection of FDLI group; (4) RT-treated group, (5) tail vein injection of FDLI plus TMH group, (6) tail vein injection of FDLI plus RT group and (7) tail vein injection of FDLI plus TMH and RT group.

According to the experimental results, the treatment intensities of the designed ACMF and RT equipment did not exert evident side effects on the mice and no notable changes in body weight or other abnormal behaviours were observed in the mice within 4 weeks after diagnosis and treatment. We first evaluated the safety of the in vivo treatment in each group. After mice from each group were sacrificed on the 16th day post-treatment, their hearts, livers, spleens, lungs and kidneys were harvested and subjected to H&E staining to evaluate the degree of damage to various organs (Figure 6A). The results revealed that no significant damage or morphological changes were detected in the major organs of mice in the control and treatment groups. This indicates that FDLI and its mediated TMH and RT are slightly toxic to the body, without causing significant damage to normal tissues during treatment. Meanwhile, blood samples were collected from each group for routine serological tests and liver and kidney function assessments (Figure 6B). The results showed that all the blood counts and the function indicators of liver and kidney were maintained at normal levels, indicating that FDLI has good safety and biocompatibility. The degrees of tumor growth inhibition in each group were preliminarily evaluated by monitoring the tumor volume (V) within 16 days (Figure 7A and B). Here the V was

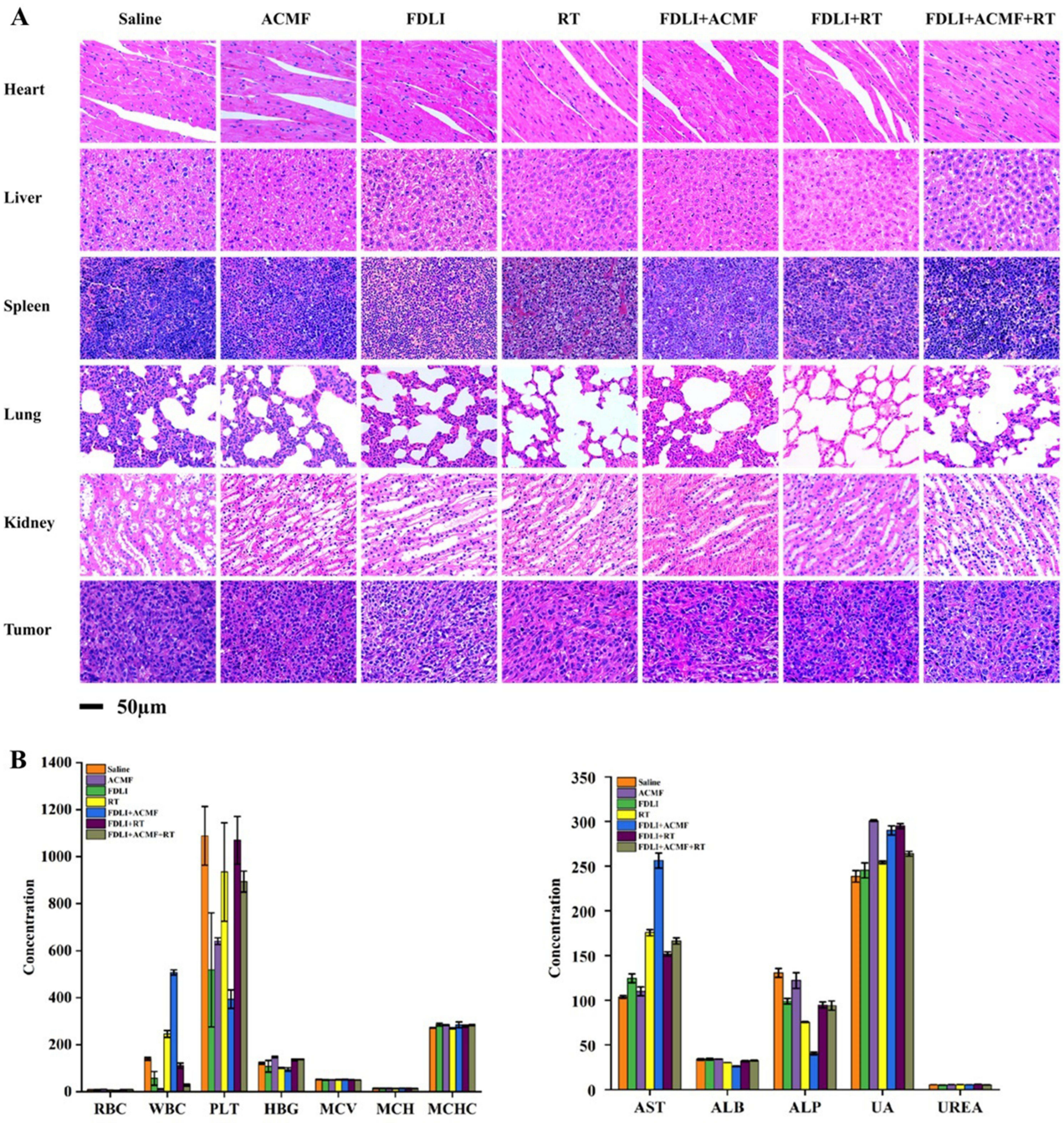

Figure 6 (**A**) H&E staining images of mice major normal organs (heart, liver, spleen, lung and kidney) and tumor tissues in the treatment of saline, ACMF, FDLI, RT, FDLI +ACMF, FDLI+RT and FDLI+ACMF+RT during a period of 16 days (8 days per stage for a total of 16 days, single dose: 20 mg/kg body weight, 200 μL per mouse). (**B**) Blood routine and liver/kidney function indicators analysis collected from mice blood at 16 days post-treatment.

calculated from the formula V = (tumor length × tumor width)2π/6. Relative tumor volume (RTV) was calculated from the formula RTV= $V/V_0 \times 100\%$. Furthermore, to compare tumor sizes across different groups and analyze the survival rates of mice in each group, we employed the independent samples *t*-test, a statistical method suitable for comparing two independent groups (eg, the treatment group vs the control group). Our results indicated that the mice in the group treated with FDLI plus ACMF and RT had the smallest tumor volume and exerted the most significant inhibitory effect. Additionally, no significant changes in body weight were observed among these groups, demonstrating that FDLI administration with TMH and RT does not noticeably impact the physical condition of the mice (Figure 7C).

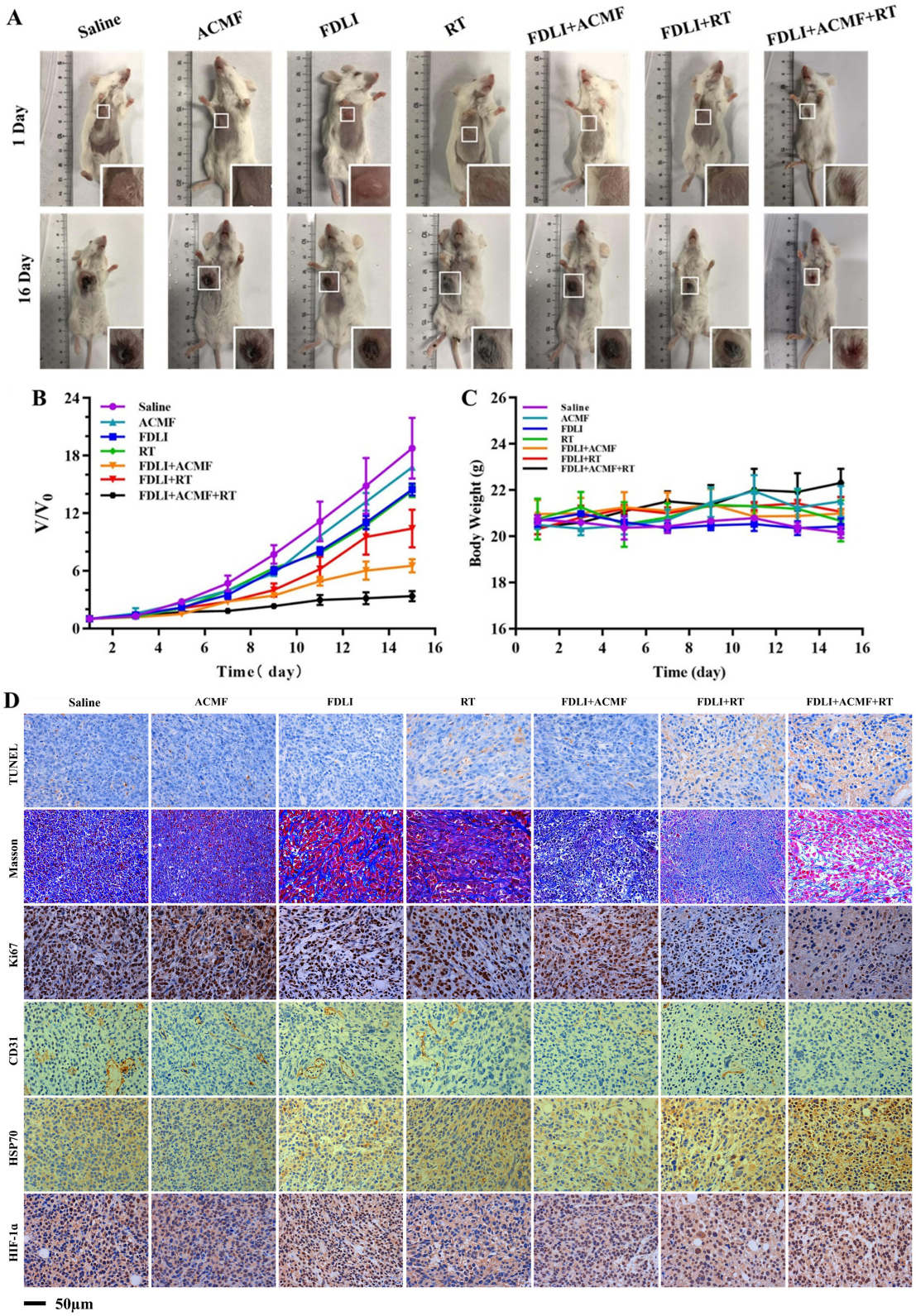

Figure 7 (**A** and **B**) Photographs of representative mice and statistical tumor volumes in different groups within 16 days (8 days per stage for a total of 16 days, single dose: 20 mg/kg body weight, 200 μL per mouse). (**C**) Body weight changes in the indicated groups during the 16 days' observation period. (**D**) IHC (TUNEL, Masson, Ki-67, CD31, HSP70 and HIF-1α) staining images of tumor sections collected from different groups at 16 days post-treatment.

https://doi.org/10.2147/IJN.S535222

To further evaluate the in vivo anti-tumor effect of FDLI-mediated combination therapy, we conducted an ex vivo histopathological study of the tumor tissue sections from each group of mice (Figures 6A and 7D). H&E staining results revealed various degrees of tumor cell damage (such as cell membrane rupture, nuclear shrinkage and fragmentation and chromatin condensation) in the group treated with FDLI plus TMH and the group treated with FDLI plus RT. However, in the group treated with FDLI plus TMH and RT, the symptoms of mouse tumor cell damage and necrosis were significantly aggravated. By contrast, tumor cells in the saline control and other treatment groups were relatively normal (Figure 6A). Furthermore, we performed TUNEL, Masson and immunohistochemical staining on the tumor sections (Figure 7D). TUNEL staining can assess the morphological characteristics of apoptotic cells through the chromatin state in the nucleus. The results showed that the proportion of apoptotic cells (indicated by brown staining signal) in the tumor tissue induced by FDLI plus TMH and RT was higher than those in the control and other treatment groups. This phenomenon was accompanied by membrane structure damage and apoptotic body formation, confirming that tumor cell apoptosis can be promoted by the combined effects. Masson staining was used to evaluate the quantity and morphology of tumor collagen fibres (blue staining) and muscle fibres (red staining) in each group to assess the tumor microenvironment. Collagen fibres are the main components of the extracellular matrix (ECM), and collagen deposition is associated with poor survival prognosis and can compress and distort tumor blood vessels, acting as a physical barrier to hinder drug delivery. The results showed that in the FDLI-mediated TMH and RT combined-treatment group, the quantity and density of the collagen and muscle fibres were significantly reduced. Different degrees of damage were also observed in the collagen and muscle cell structures, indicating that the minimal ECM-induced compression of tumor blood vessels promotes FDLI infiltration into tumor tissues and enhances therapeutic efficacy. Furthermore, immunohistochemical staining on HIF-1α, CD31, Ki-67 and HSP70 protein indicators of tumor tissues in each group was conducted to evaluate the influence of the treatment on tumor hypoxic environment, anti-angiogenesis, cell proliferation and migration. Generally, the sensitivity of tumor cells to RT is reduced by the presence of a hypoxic environment in solid tumors. Our results showed that HIF-1α protein expression (brown staining) was significantly reduced after FDLI administration and combined treatment. This finding demonstrates that FDLI-mediated combination therapy can improve the tumor hypoxic environment and increase the sensitivity of tumor cells to radiation, thereby enhancing the tumor killing effect. Additionally, CD31 and Ki67 staining results showed that FDLI-mediated combination therapy delayed cell proliferation and migration to the greatest extent and inhibited tumor microvessels. HSP70 staining results revealed that FDLI-mediated combination therapy produced significant thermal stimulation in tumor tissues to induce anti-tumor immune responses and improve anti-tumor efficacy.

Proteins were extracted from the tumor tissues of mice in each group and subjected to WB experiments to further validate the molecular mechanism of FDLI-mediated combined anti-tumor effects. The following proteins were selected for investigation (Figure 8A–E): Bax and Bcl-2, related to mitochondrial apoptosis; γ-H2A.X, related to DNA damage sensitivity and repair ability; and GPX4, related to ferroptosis. Unprocessed and completed above WB result of β-Actin, Bax, Bcl-2, γ-H2A.X and GPX4 protein were also shown in Figures S4–S8. Compared with the other groups, the FDLI-mediated TMH and RT combined treatment significantly inhibited the expression of the anti-apoptotic protein Bcl-2 and increased the expression of the pro-apoptotic protein Bax in the tumor tissues, indicating its promoting effect on tumor cell apoptosis. The GSH system in tumor cells can eliminate intracellular ROS to prevent oxidative damage to cells by ROS and is crucial in maintaining intracellular redox stability. Additionally, GSH can assist GPX4 in reducing toxic LPO to non-toxic hydroxyl compounds (LOHs) to prevent LPO-induced damage to membrane structure and function, which is significantly associated with the triggering of “ferroptosis”. The results showed that FDLI-mediated TMH and RT combined treatment reduced GPX4 protein expression to varying degrees, indicating that ferroptosis may also be a route for inducing tumor cell death. Moreover, γ-H2A.X is a key regulatory factor of cellular DNA damage. It can promote DNA damage repair in normal cells but facilitate the accumulation of DNA damage in tumor cells. The main damage caused by RT to tumor cells is DNA damage, and a high γ-H2A.X level can be used to indicate tumor cell sensitivity to RT. The results demonstrated that FDLI administration and its combined treatment with TMH and RT significantly increased γ-H2A.X expression, indicating increased DNA damage in tumor cells and enhanced sensitivity to RT.

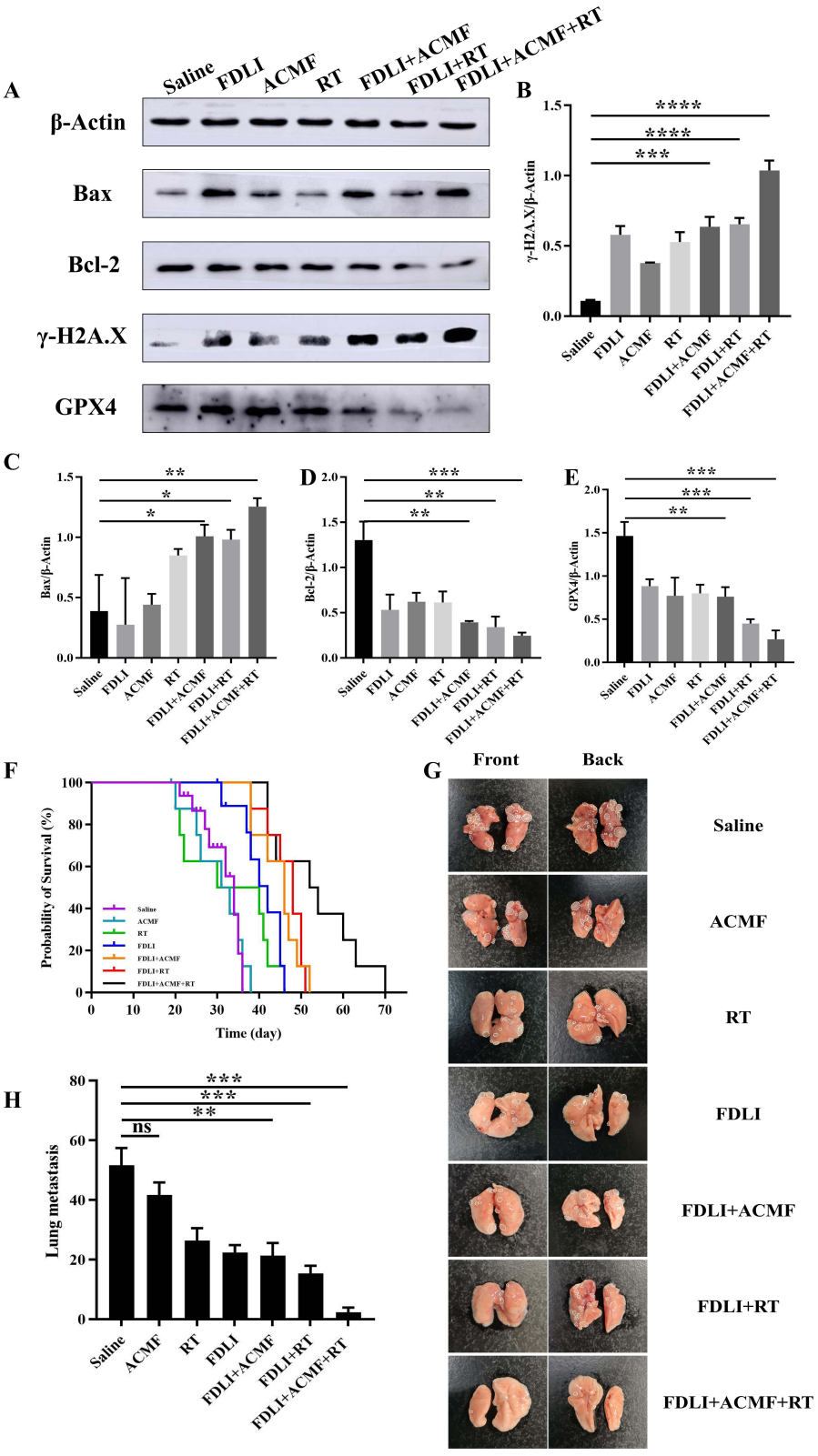

Figure 8 (**A**–**E**) Proteins were extracted from the tumor tissues of mice in each group and subjected to WB experiments (Bax, Bcl-2, γ-H2A.X, and GPX4). (**F**) Survival curves of mice in different treatments. (**G** and **H**) Photograph and statistics of lung metastatic nodules in each group (*p < 0.05, **p< 0.01, ***p < 0.001, ****P<0.0001).

https://doi.org/10.2147/IJN.S535222

Evaluation of Lung Metastasis and Survival Rate

During the treatment, the lifespan of mice was also monitored (Figure 8F). Compared with the control and other groups, the lifespan of the mice receiving FDLI-mediated combination treatment was extended to more than 43 days. Thus, the survival rate was significantly improved. The maximum lifespan of the mice treated by FDLI combined with ACMF and RT can exceed 70 days. To determine whether the FDLI-mediated combination effect can inhibit the distant metastasis of tumor cells at the histological level, we continued the treatment in mice for a specified period and then dissected them to obtain their lung tissue. We counted the number of nodules and observed tumor cell metastasis (Figure 8G and H). Compared with the control and other groups, the number of lung nodules in the group treated by the combination therapy was significantly reduced without any evident metastatic tumor lesions, indicating that combination therapy can greatly improve the inhibition of tumor metastasis in the mice.

As a magnetic fluid capable of targeting mitochondria, FDLI not only leverages the safety performance and superparamagnetism of Fe_3O_4 as a traditional magnetothermal material but also integrates the current research findings on targeted mitochondrial therapy for antitumor treatment. By utilizing its targeting and magnetothermal properties, FDLI enables nanomaterials to achieve excellent intracellular magnetothermal therapeutic effects while enhancing the sensitivity of tumor cells to RT. Additionally, it exhibits strong imaging capabilities, providing a new approach for the diagnosis and treatment of TNBC. The combination of TMH and RT not only clarifies the tumor RT target area more precisely and improves the accuracy of RT but also promotes ferroptosis in tumor cells during the magnetothermal process, thereby enhancing the sensitivity of tumors to radiation.

Conclusion

In this study, a high-performance FDLI probe was developed, which exhibited remarkable fluorescence emission properties and mitochondria-specific active targeting ability. Under tumor cell-mediated endocytosis, TMH can be fully enriched in localised cells and simultaneously exert enzyme-like activity to generate large amounts of toxic ·OH, providing a precise and intelligent targeted drug delivery mode for efficient tumor therapy. Meanwhile, FDLI targets and destroys mitochondrial structures, reduces cellular ATP production and increases intracellular ROS levels. The decreased GSH levels lead to increased MDA levels. Accordingly, ferroptosis is induced in the tumor cells, leading to improved RT sensitivity. The FDLI-mediated TMH and RT combined therapy effectively controls tumor cell metastasis and inhibits tumor growth, thereby prolonging the lifespan of mice. This approach demonstrates greater potential for clinical application than therapy with TMH or RT alone and provides a solid foundation for improving the integration of tumor diagnosis and treatment.

Acknowledgments

This research was supported by the National Natural Science Foundation of China (81672973, 81701821), Major Fundamental Research Program of Natural Science Foundation of Jiangsu Higher Education Institution of China (16KJB310003), Jiangsu Provincial Natural Science Foundation General Project (BK20241767), Xuzhou Medical Leading Talent Project (XWRCHT2021002) and Beijing Medical Public Welfare Foundation Project (DY-Tumor 2022-1003).

Disclosure

There are no conflicts to declare.

References

1. Ma Z, Mohapatra J, Wei K, et al. Magnetic nanoparticles: synthesis, anisotropy, and applications. *Chem Rev*. 2023;123(7):3904–3943. doi:10.1021/acs.chemrev.1c00860
2. Li X, Liu X, Liu X. Self-assembly of colloidal inorganic nanocrystals: nanoscale forces, emergent properties and applications. *Chem Soc Rev*. 2021;50:2074–2101. doi:10.1039/D0CS00436G
3. Turrina C, Schoenen M, Milani D, et al. Application of magnetic iron oxide nanoparticles: thrombotic activity, imaging and cytocompatibility of silica-coated and carboxymethyl dextrane-coated particles. *Colloid Surf B*. 2023;228:113428. doi:10.1016/j.colsurfb.2023.113428

4. Gavilán H, Avugadda SK, Fernández-Cabada T, et al. Magnetic nanoparticles and clusters for magnetic hyperthermia: optimizing their heat performance and developing combinatorial therapies to tackle cancer. *Chem Soc Rev*. 2021;50:11614–11667. doi:10.1039/d1cs00427a
5. Picchi DF, Biglione C, Horcajada P. Nanocomposites based on magnetic nanoparticles and metal-organic frameworks for therapy, diagnosis, and theragnostics. *ACS Nanosci Au*. 2024;4(2):85–114. doi:10.1021/acsnanoscienceau.3c00041
6. Soetaert F, Korangath P, Serantes D, et al. Cancer therapy with iron oxide nanoparticles: agents of thermal and immune therapies. *Adv Drug Deliv Rev*. 2020;163–164:65–83. doi:10.1016/j.addr.2020.06.025
7. Zhu Y, Li Q, Wang C, et al. Rational design of biomaterials to potentiate cancer thermal therapy. *Chem Rev*. 2023;123(11):7326–7378. doi:10.1021/acs.chemrev.2c00822
8. Kok HP, Cressman ENK, Ceelen W, et al. Heating technology for malignant tumors: a review. *Int J Hyperther*. 2020;37(1):711–741. doi:10.1080/02656736.2020.1779357
9. Sohail A, Ahmad Z, Bég OA, et al. A review on hyperthermia via nanoparticle-mediated therapy. *Bull Cancer*. 2017;104(5):452–461. doi:10.1016/j.bulcan.2017.02.003
10. Lee JH, Jang JT, Choi JS, et al. Exchange-coupled magnetic nanoparticles for efficient heat induction. *Nat Nanotechnol*. 2011;6(7):418–422. doi:10.1038/nnano.2011.95
11. Beola L, Asín L, Roma-Rodrigues C, et al. The intracellular number of magnetic nanoparticles modulates the apoptotic death pathway after magnetic hyperthermia treatment. *ACS Appl Mater Inter*. 2020;12(39):43474–43487. doi:10.1021/acsami.0c12900
12. Jang JT, Lee J, Seon J, et al. Giant magnetic heat induction of magnesium-doped γ-Fe_2O_3 superparamagnetic nanoparticles for completely killing tumors. *Adv Mater*. 2018;30(6):1–8 doi:10.1002/adma.201704362
13. Wu WS, Yan X, Chen S, et al. Minimally invasive delivery of percutaneous ablation agent via magnetic colloidal hydrogel injection for treatment of hepatocellular carcinoma. *Adv Mater*. 2024;36(26):e2309770. doi:10.1002/adma.202309770
14. Ying W, Zhang Y, Gao W, et al. Hollow magnetic nanocatalysts drive starvation-chemodynamic-hyperthermia synergistic therapy for tumor. *ACS Nano*. 2020;14(8):9662–9674. doi:10.1021/acsnano.0c00910
15. Gupta R, Chauhan A, Kaur T, et al. Enhancing magnetic hyperthermia efficacy through targeted heat shock protein 90 inhibition: unveiling immune-mediated therapeutic synergy in glioma treatment. *ACS Nano*. 2024;18(26):17145–17161. doi:10.1021/acsnano.4c03887
16. Prokopiou DE, Chillà A, Margheri F, et al. Iron oxide nanoparticles: selectively targeting melanoma cells in vitro by inducing DNA damage via H2AX phosphorylation and hindering proliferation through ERK dephosphorylation. *Pharmaceutics*. 2024;16(4):527. doi:10.3390/pharmaceutics16040527
17. Mansur AAP, Mansur HS, Leonel AG, et al. Supramolecular magnetonanohybrids for multimodal targeted therapy of triple-negative breast cancer cells. *J Mater Chem B*. 2020;8:7166–7188. doi:10.1039/D0TB01175D
18. Zhao P, Zhao J, Deng Y, et al. Application of iron/barium ferrite/carbon-coated iron nanocrystal composites in transcatheter arterial chemoembolization of hepatocellular carcinoma. *J Colloid Interf Sci*. 2021;601:30–41. doi:10.1016/j.jcis.2021.05.102
19. Yang N, Gong F, Cheng L, et al. Biodegradable magnesium alloy with eddy thermal effect for effective and accurate magnetic hyperthermia ablation of tumors. *Natl Sci Rev*. 2021;8(1):nwaa122. doi:10.1093/nsr/nwaa122
20. Ahmed M, Brace CL, Lee FT, et al. Principles of and advances in percutaneous ablation. *Radiology*. 2011;258(2):351–369. doi:10.1148/radiol.10081634
21. Chu KF, Dupuy DE. Thermal ablation of tumours: biological mechanisms and advances in therapy. *Nat Rev Cancer*. 2014;14(3):199–208. doi:10.1038/nrc3672
22. Qin Q, Zhou Y, Li P, et al. Phase-transition nanodroplets with immunomodulatory capabilities for potentiating mild magnetic hyperthermia to inhibit tumour proliferation and metastasis. *J Nanobiotechnology*. 2023;21:131. doi:10.1186/s12951-023-01885-4
23. Mai BT, Fernandes S, Balakrishnan PB, et al. Nanosystems based on magnetic nanoparticles and thermo- or pH-responsive polymers: an update and future perspectives. *Accouts Chem Res*. 2018;51(5):999–1013. doi:10.1021/acs.accounts.7b00549
24. Cheng CA, Chen W, Zhang L, et al. A responsive mesoporous silica nanoparticle platform for magnetic resonance imaging-guided high-intensity focused ultrasound-stimulated cargo delivery with controllable location, time, and dose. *J Am Chem Soc*. 2019;141(44):17670–17684. doi:10.1021/jacs.9b07591
25. Cho HY, Lee T, Yoon J, et al. Magnetic oleosome as a functional lipophilic drug carrier for cancer therapy. *ACS Appl Mater Inter*. 2018;10(11):9301–9309. doi:10.1021/acsami.7b19255
26. Zhou S, Tsutsumiuchi K, Imai R, et al. In vitro study of tumor-homing peptide-modified magnetic nanoparticles for magnetic hyperthermia. *Molecules*. 2024;29(11):2632. doi:10.3390/molecules29112632
27. Liu S, Shi D, Chen L, et al. Paclitaxel-loaded magnetic nanocrystals for tumor neovascular-targeted theranostics: an amplifying synergistic therapy combining magnetic hyperthermia with chemotherapy. *Nanoscale*. 2021;13:3613–3626. doi:10.1039/D0NR08197C
28. Wang J, Chen P, Dong Y, et al. Designer exosomes enabling tumor targeted efficient chemo/gene/photothermal therapy. *Biomaterials*. 2021;276:121056. doi:10.1016/j.biomaterials.2021.121056
29. Balasubramanian S, Girija AR, Nagaoka Y, et al. Curcumin and 5-fluorouracil-loaded, folate- and transferrin-decorated polymeric magnetic nanoformulation: a synergistic cancer therapeutic approach, accelerated by magnetic hyperthermia. *Int J Nanomed*. 2014;9:437–459. doi:10.2147/IJN.S49882
30. Min T, Yang C, Zhang M, et al. Mild magnetothermal immunotherapy for malignant pleural effusion. *Small*. 2024;8:e2407734 doi:10.1002/smll.202407734
31. Vakifahmetoglu-Norberg H, Ouchida AT, Norberg E. The role of mitochondria in metabolism and cell death. *Biochem Biophys Res Commun*. 2017;482(3):426–431. doi:10.1016/j.bbrc.2016.11.088
32. Balaban RS, Nemoto S, Finkel T. Mitochondria, oxidants, and aging. *Cell*. 2005;120(4):483–495. doi:10.1016/j.cell.2005.02.001
33. Vercellino I, Sazanov LA. The assembly, regulation and function of the mitochondrial respiratory chain. *Nat Rev Mol Cell Bio*. 2022;23(2):141–161. doi:10.1038/s41580-021-00415-0
34. Malhotra J, Xiong M, Miao H, et al. Endoplasmic reticulum to mitochondria Ca^{2+} signaling inhibits Factor VIII secretion and mediates oxidative stress and apoptosis upon Factor VIII expression. *Blood*. 2010;116(21):2212. doi:10.1182/blood.V116.21.2212.2212
35. Wozny MR, Di Luca A, Morado DR, et al. In situ architecture of the ER-mitochondria encounter structure. *Nature*. 2023;618(7963):188–192. doi:10.1038/s41586-023-06050-3

36. Zhang R, Zhang L, Ran H, et al. A mitochondria-targeted anticancer nanoplatform with deep penetration for enhanced synergistic sonodynamic and starvation therapy. *Biomater Sci*. 2020;8(16):4581–4594. doi:10.1039/D0BM00408A
37. Yang Z, Wang J, Liu S, et al. Defeating relapsed and refractory malignancies through a nano-enabled mitochondria-mediated respiratory inhibition and damage pathway. *Biomaterials*. 2020;229:119580. doi:10.1016/j.biomaterials.2019.119580
38. Dixon SJ, Olzmann JA. The cell biology of ferroptosis. *Nat Rev Mol Cell Bio*. 2024;25(6):424–442. doi:10.1038/s41580-024-00703-5
39. Tang D, Chen X, Kang R, et al. Ferroptosis: molecular mechanisms and health implications. *Cell Res*. 2021;31(2):107–125. doi:10.1038/s41422-020-00441-1
40. Dixon SJ, Lemberg KM, Lamprecht MR, et al. Ferroptosis: an iron-dependent form of nonapoptotic cell death. *Cell*. 2012;149(5):1060–1072. doi:10.1016/j.cell.2012.03.042
41. Zhou H, Liu Z, Zhang Z, et al. Copper-cysteamine nanoparticle-mediated microwave dynamic therapy improves cancer treatment with induction of ferroptosis. *Bioact Mater*. 2022;24:322–330. doi:10.1016/j.bioactmat.2022.12.023
42. Deng X, Liu T, Zhu Y, et al. Ca & Mn dual-ion hybrid nanostimulator boosting anti-tumor immunity via ferroptosis and innate immunity awakening. *Bioact Mater*. 2023;33:483–496. doi:10.1016/j.bioactmat.2023.11.017
43. Liang X, Chen M, Bhattarai P, et al. Complementing cancer photodynamic therapy with ferroptosis through iron oxide loaded porphyrin-grafted lipid nanoparticles. *ACS Nano*. 2021;15(12):20164–20180. doi:10.1021/acsnano.1c08108
44. Tang Q, Wang Y, Yan B, et al. Intracellular magnetic hyperthermia sensitizes sorafenib to orthotopic hepatocellular carcinoma via amplified ferroptosis. *ACS Nano*. 2024;18(43):29804–29819. doi:10.1021/acsnano.4c09500
45. Xie J, Yan C, Zhang Y, et al. Shape evolution of "multibranched" Mn−Zn ferrite nanostructures with high performance: a transformation of nanocrystals into nanoclusters. *Chem Mater*. 2013;25(18):3702–3709. doi:10.1021/cm402036d
46. Xie J, Zhang Y, Yan C, et al. High-performance PEGylated Mn–Zn ferrite nanocrystals as a passive-targeted agent for magnetically induced cancer theranostics. *Biomaterials*. 2014;35(33):9126–9136. doi:10.1016/j.biomaterials.2014.07.019
47. Xie J, Yan C, Yan Y, et al. Multi-modal Mn–Zn ferrite nanocrystals for magnetically-induced cancer targeted hyperthermia: a comparison of passive and active targeting effects. *Nanoscale*. 2016;8(38):16902–16915. doi:10.1039/C6NR03916B

International Journal of Nanomedicine

Dovepress
Taylor & Francis Group

Publish your work in this journal

The International Journal of Nanomedicine is an international, peer-reviewed journal focusing on the application of nanotechnology in diagnostics, therapeutics, and drug delivery systems throughout the biomedical field. This journal is indexed on PubMed Central, MedLine, CAS, SciSearch®, Current Contents®/Clinical Medicine, Journal Citation Reports/Science Edition, EMBase, Scopus and the Elsevier Bibliographic databases. The manuscript management system is completely online and includes a very quick and fair peer-review system, which is all easy to use. Visit http://www.dovepress.com/testimonials.php to read real quotes from published authors.

Submit your manuscript here: https://www.dovepress.com/international-journal-of-nanomedicine-journal